

# Massive sediment pulses triggered by a multi-stage alpine cliff fall (Hochvogel, DE/AT)

Natalie Barbosa<sup>1,2</sup>, Johannes Leinauer<sup>2</sup>, Juilson Jubanski<sup>3</sup>, Michael Dietze<sup>4,5</sup>, Ulrich Münzer<sup>6</sup>, Florian Siegert<sup>1,3</sup>, Michael Krautblatter<sup>2</sup>.

- 5 <sup>1</sup>Department of Earth and Environmental Sciences, Faculty of Earth Sciences, GeoBio Center, Ludwig-Maximilians-University, Munich, 80333, Germany.  
<sup>2</sup>Chair of Landslide Research, Technical University of Munich, Munich, 80333, Germany  
<sup>3</sup>3D RealityMaps GmbH, Munich, 81673, Germany  
<sup>4</sup>Faculty of Geosciences and Geography, Georg-August-Universität Göttingen, Göttingen, 31073, Germany  
10 <sup>5</sup>GFZ German Research Centre for Geosciences, Potsdam, 14473, Germany  
<sup>6</sup>Department of Earth and Environmental Sciences, Section Geology, Ludwig-Maximilians-University, Munich, 80333, Germany.

Correspondence to: Natalie Barbosa ([barbosa@biologie.uni-muenchen.de](mailto:barbosa@biologie.uni-muenchen.de))

## 15 Abstract

Massive sediment pulses in catchments are a key alpine multi-risk component. Substantial sediment redistribution in alpine catchments frequently causes flooding, river erosion, and landsliding, and affects infrastructure such as dam reservoirs as well as aquatic ecosystems and water quality. While systematic rock slope failure inventories have been collected in several countries, the subsequent cascading sediment redistribution is virtually unaccessed.

20 This contribution reports for the first time the massive sediment redistribution triggered by the multi-stage failure of more than 150,000 m<sup>3</sup> from the Hochvogel dolomite peak during the summer of 2016. We applied change detection techniques on seven 3D-coregistered high-resolution true-orthophotos and digital surface models (DSM) obtained through digital aerial photogrammetry later optimized for precise volume calculation in steep terrain. The analysis of seismic information from surrounding stations revealed the temporal evolution of the cliff fall.

25 We identified the proportional contribution of >600 rockfall events (>1 m<sup>3</sup>) from 4 rock slope catchments with different aspects and their volume estimates. In a sediment cascade approach, we evaluated erosion, transport, and deposition from the rockface to the upper channelized erosive debris flow channel, then to the widened dispersive debris flow channel, and finally to the outlet into the braided sediment-supercharged Jochbach river. We observe the decadal flux of- more than 400,000 m<sup>3</sup> of sediment, characterized by massive sediment waves ~~with massive~~

30 ~~sediment pulses~~ that (i) respond exhibit with reaction times of 0-4 years in response to a cliff fall sediment input, and relaxation times beyond 10 years, (ii) manifest with faster response times of 0-2 years in the upper catchment and more than over 2 years response times in the lower catchments, (iii) undergo a rapid shift from the inversion ~~of~~ sedimentary (10<sup>2</sup>-10<sup>3</sup> mm/a) to massive erosive regimes (10<sup>2</sup> mm/a) within single years and ~~the~~ (iv) show limited dependency ~~of redistribution~~ to rainfall frequency and intensity. This study provides generic information

35 on spatial and temporal patterns of massive sediment pulses in highly sediment-charged alpine catchments.

## Keywords

large format aerial photogrammetry, ~~rockfall~~, massive sediment redistribution, increased debris flow activity,  
40 alpine catchment, Hochvogel.

## 1 Introduction

45

Recent high-magnitude rockfalls in the European Alps raised attention to the potential of catastrophic cascading sediment transport and their societal impact (e.g., Piz Cengalo Bergsturz (Baer et al., 2017).

50

Sediment cascades define the dynamic process of sediment mobilization and deposition within a landscape that encompasses the continuous travel of sediment particles from their source, through the river network, and to eventual deposition in sediment sinks (Burt and Allison, 2010). Key driven processes to sediment cascades are landslides and rockfalls acting as sources of sediment, and debris flows and sediment transport as mechanisms of sediment remobilization. Mechanisms and scales of sediment propagation throughout space and time in sediment cascades are paramount to the development of prevention and mitigation measures. Several A handful of studies

55

have focused on sediment cascades on active mountain environments controlled by landsliding (e.g., Benda and Dunne, 1997; Wichmann et al., 2009; Bennett et al., 2013; Heckmann et al., 2016; Clapuyt et al., 2019) as - Landslides provide and condition the input of sediment volumes into the sediment cascade. -Despite their relevance in the sediment cascades, landslide deposit residence times, cascade sediment pulses, and redistribution controlling factors are rarely quantified due to the sudden, unpredictable, and spatially distributed occurrence.

60

Sediment delivery from rockfalls to the drainage network has significant implications for catchment scale sediment fluxes and landform evolution (Benda and Dunne, 1997; Tucker, 2004). -Despite this, there is a lack of systematic studies focused on the short term temporal and spatial development of mechanisms that link and maintain sediment continuity within hillslopes. Attempts to better understand short termdecadal to centennial

65

erosion rates and sediment yield at a basin scale include geomorphological observations and spatial pattern analysis (Schrott et al., 2003; Theler et al., 2010), monitoring of sediment fluxes and construction of sediment budgets (Dietrich et al., 1982; Becht et al., 2009; Brown et al., 2009; Heckmann et al., 2016; Joyce et al., 2018)(Joyce et al., 2018), numerical modeling (Wichmann et al., 2009; Heckmann and Schwanghart, 2013; Bennett et al., 2014; Battista et al., 2022)(Wichmann et al., 2009; Heckmann and Schwanghart, 2013), -and

70

application of the connectivity framework (Borselli et al., 2008; Fryirs, 2013; Heckmann and Schwanghart, 2013; Bracken et al., 2015)(Wichmann et al., 2009; Fryirs, 2013). These approaches incorporate both spatial and temporal variability in the operation of the sediment cascades at a diversity of scales, however, they lack key observations on rare and high-magnitude events and the subsequent sediment transfer at high spatial resolutions.-

75

A disturbance in terms of landscape dynamics, is an event fairly extreme that produces a measurable response in the rate or type of processes occurring in the landscape. The system response time to a disturbance is the combination of the reaction time, the time needed for a system to start responding, and relaxation time, the time taken for the system to complete the response and adjust to the change. Short reaction times are of particular concern, while long relaxation times expand the temporal activity of processes that might result in catastrophic

80

societal outputs (Owens et al., 2010) for example, debris flows. Recent high magnitude rockfalls in the European Alps raised attention to the potential of catastrophic cascading sediment transport. The 2011 and 2017 rockslides in the upper Val Bondasca, Swiss Alps, were preceded by an unusually high debris flow activity that reached the

~~town of Bondo (Baer et al., 2017; Mergili et al., 2020). A total of 99 buildings were damaged by the multiple debris flows that occurred on August 2017 with an assumed economical loss of around 41 million francs (NNZ,~~

85 ~~2017). On the other hand, D~~ debris flows serve as a link to hillslope-channel coupling by connecting large parts of rock walls to the channel network (Heckmann and Schwanghart, 2013; Bennett et al., 2014). Debris flows rapidly mobilize  $< 10^2$  to  $> 10^9$  m<sup>3</sup> of sediment (Jakob, 2005) along great distances reaching infrastructure and populated areas. While debris flows are typically considered transport-limited processes (Gregory and Lewin, 2014), numerical simulations suggest that continuous delivery of sediment from upslope areas to the location where  
90 debris flows are initiated maintains the supply of material available for transport, thus, impacting the persistence and magnitude of sediment pulses in the system (Heckmann and Schwanghart, 2013)(~~Heckmann and Schwanghart, 2013~~). Several studies have collected data from massive rock slope failures (e.g., Dussauge-Peisser et al., 2002; Heckmann et al., 2012; Fischer et al., 2012; Krautblatter et al., 2012; Guerin et al., 2020) which are a major landscape evolution process and significantly contribute to sediment yields by sporadic production of a  
95 considerable ( $< 10^3$  m<sup>3</sup> km<sup>2</sup> yr<sup>-1</sup>) amount of debris (McSaveney, 2002; Korup et al., 2010; Krautblatter et al., 2012).

~~In the coming decades with enhanced rainstorm activity, massive sediment redistribution primarily by debris flows in alpine catchments will be a key hazard and challenge in alpine communities, thus, constraining rates and sediment cascades response times to suddenly increased sediment input by landsliding is paramount for prediction and early warning. However, few studies have quantitatively assessed the subsequent cascading sediment  
100 redistribution and reaction and relaxation times in highly active alpine catchments. Recent high magnitude rockfalls in the European Alps raised attention to the potential of catastrophic cascading sediment transport. The 2011 and 2017 rockslides in the upper Val Bondasca, Swiss Alps, were preceded by an unusually high debris flow activity that reached the town of Bondo (Baer et al., 2017; Mergili et al., 2020). A total of 99 buildings were damaged by the multiple debris flows that occurred on August 2017 with an assumed economical loss of around  
105 41 million francs (NNZ, 2017). In the coming decades with enhanced rainstorm activity, massive sediment redistribution in alpine catchments will be a key hazard and challenge in alpine communities, thus, constraining rates and sediment cascades response times to suddenly increased sediment input by landsliding is paramount for prediction and early warning.~~

110

~~Developments in digital photogrammetry allow the 3D reconstruction of landscapes from images taken using a diversity of platforms (Eltner and Sofia, 2020). Large format digital photogrammetry with (multi-)year temporal resolution and high-spatial resolution (20 cm) covering vast areas, presents a valuable, yet unexplored, data source for geomorphic changes in the last decade. Reconstruction of elevation models from nadir-view images in  
115 mountainous landscapes is challenging (Fawcett et al., 2019). Photogrammetric models of steep terrain and pseudo-vertical walls include random errors still difficult to minimize and quantify accurately, yet allow the unlock of a historical perspective and provide insights on sediment cascade spatial patterns in climate-sensitive landscapes (e.g., Fabris and Pesci, 2009; Berger et al., 2011; Bennett et al., 2012; Savi et al., 2023). Despite the temporal resolution that results in the coalescence of events, a combination of techniques such as high-resolution  
120 seismic investigation provides a potential complement to the photogrammetric record.~~

This paper reports the massive sediment redistribution triggered by the multi-stage failure from the Hochvogel dolomite peak during the summer of 2016. We evaluate the spatio-temporal morphodynamics at a catchment scale before and after the cliff fall by means of multi-temporal high-resolution aerial photogrammetry between 2010 and 2020. The (multi-) annual photogrammetric surveys provide information on detachment areas and failed volumes. ~~Still, but the time-temporal resolution is limited to the recurrence interval between two consecutive consecutive surveys surveys, i.e., one to two years. We do not intend to resolve single events but rather decipher rockfall patterns and catchment sediment dynamics after an unusual sediment input to the catchment. To overcome this limitation, we~~ Additionally, we complement the understanding of a single rockfall event by the use of high-resolution seismic records capturing relevant rockfall events (e.g., Hibert et al., 2011; Lacroix and Helmstetter, 2011; Manconi et al., 2016; Fuchs et al., 2018; Dietze et al., 2017a). The combination of seismic information with high-resolution wide-extent photogrammetric reconstructions resulted in (i) identification of the spatial and temporal contribution of rockfall material from the four rock slope catchments that constitute the Hochvogel summit, (ii) quantification of (multi-) annual series of sediment budgets erosion rates before and after the cliff fall evidencing the dramatic inversion of deposition and erosion processes, (iii) time series of sediment cascading and (iv) estimation of the system reaction time and redistribution controls with respect to rainstorm intensity and frequencies. To our knowledge, this paper is the one of few publications first to showing the cascading sediment response of an alpine catchment to a massive rock slope failure. This enables a better understanding of catchment morphodynamic responses to high magnitude rock fall, propagation, and persistence of sediment waves through alpine catchment system and future hazard scenarios where increased sediment availability and seasonal extreme heavy rainfall are expected.

## 2 Study area

The Hochvogel peak (47°21'N, 10°26'E, 2,592 m a.s.l), is a prominent summit in the Northern Calcareous Alps and a popular destination for hikers. The Hochvogel massif consists of Hauptdolomit, a brittle, variably bituminous carbonate rock with pronounced bedding (dm-m) and incidental marly interlayers. The rock mass is tectonically stressed and highly weathered. A meter-size fracture at the summit poses a catastrophic rock failure scenario (Leinauer et al., 2020, 2021) directly impacting the Weittal valley (Figure 1).

Four slopes constitute the pyramidal-shaped summit with orientations towards northeast, west, southeast, and southwest and mean inclinations between 43° to 47°. The southwestern slope is distinguished by its current almost vertical wall and upper negative slope reaching the peak of the summit. Slope processes occurring at the southwestern slope are transferred to the Weittal catchment which extends over 1.9 km<sup>2</sup> with an elevation difference of more than 1,300 m. The area directly affected by slope instabilities occurring at the southwestern slope covers 378,642 m<sup>2</sup> between 2010 to 2021 and is divided into four morpho-dynamic components-zones (Figure 1a) **rock face:** with strong slope changes, serve as the source of sediment production (primary and secondary rockfalls), **upper channelized erosive debris flow channel:** characterized by a mean slope of 42°, promotes temporal accumulation of sediment in an incipient slope talus. A confined asymmetric valley follows the slope talus limited to the east by vertical walls of almost 60 m in height. At the same time, to the west, sporadic minor pulses of sediment are produced by erosion of the base of an older slope deposit gently oriented southwest.

160 **widened dispersive debris flow channel:** geographically limited by the intersection of the Weittal and Wildenbach streams, starts by a rock wall confined valley which transforms into a highly active unconfined slope under continuous incision of older deposits and the **outlet** into the Jochbach river which imposes a high sediment transfer regime evidenced in the braided development of the river along an alluvial plain with a mean inclination of 14° and the presence of terraces with a height between 1 to 3 m from the current main channel.

165

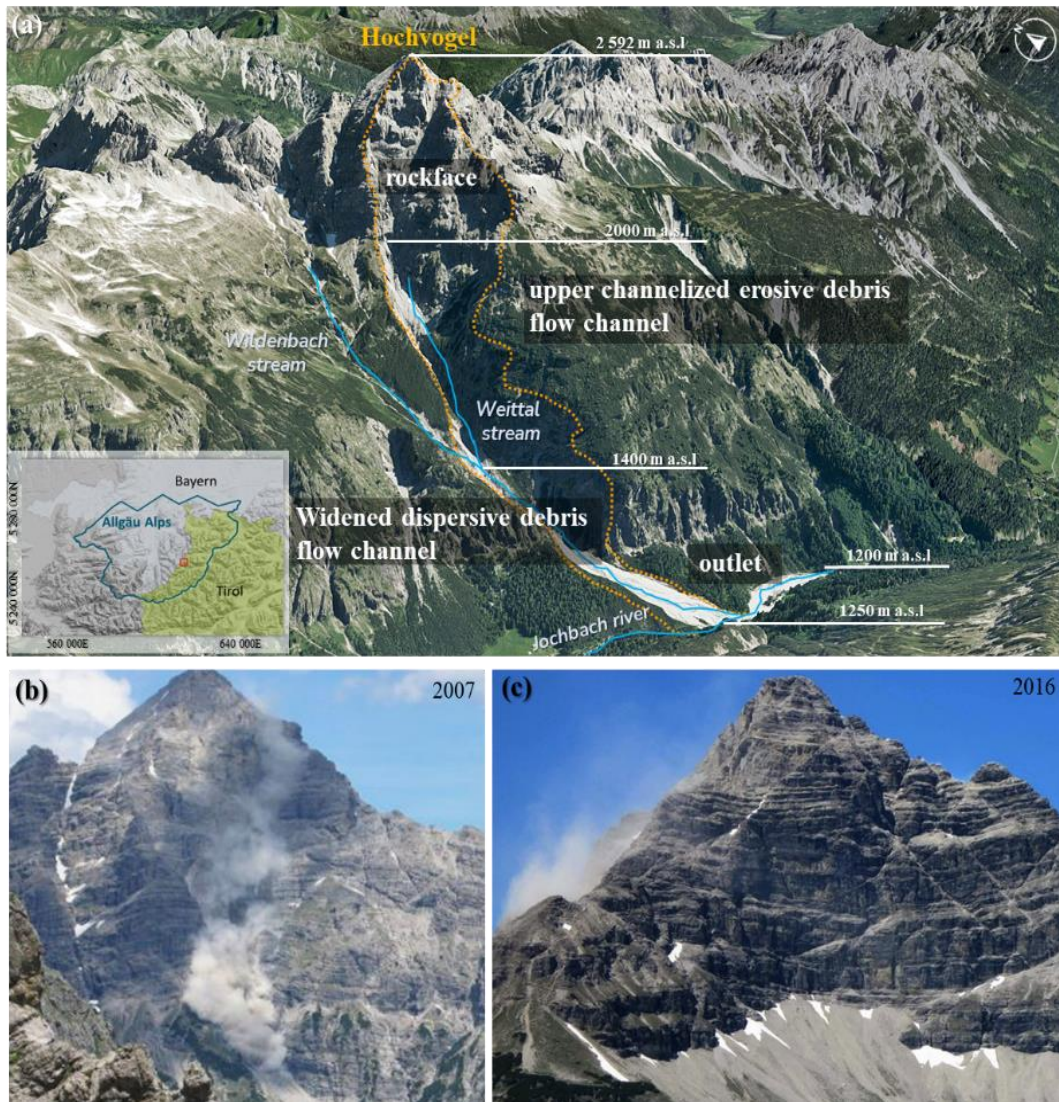
Rockfalls on the southeastern and southwest slopes of the Hochvogel summit were documented in 1934, 1935, 2005, and 2007 (DAV, 2017). Between Saturday 9 and Monday 11 of July 2016 (Heißel and Figl, 2017), noises and a dust cloud alerted the local authorities due to a new rockfall event that affected the Weittal valley (Figure 1. b and c.).

## 170 **3. Methods**

### **3.1 Multi-temporal quantification of surface change**

175 We used large format aerial imagery surveyed by the Austrian and German Cartographic Survey offices (BEV & LDBV) and by 3D RealityMaps GmbH to investigate the spatial and temporal sediment production, transport, and accumulation patterns of the southwest slope of the Hochvogel in 6 intervals over ten years. All seven surveys (09.2010, 08.2012, 09.2014, 06.2015, 08.2017, 09.2018, and 08.2020) have a nominal 20 cm spatial resolution (supplementary Table 1.) for the production of the digital surface models (DSM) and true orthophotos from the photogrammetric point clouds. The produced DSMs were aligned to the reference dataset acquired on 21.09.2018 by means of a 3D-coregistration for the further application of change detection and volume calculation.





180

Figure 1. a) Location of the Hochvogel summit in the Allgäu Alps between Bavaria (Germany) and Tirol (Austria) and 3D-reconstruction of the southwest slope indicating the approximate elevation of the boundaries of the morphodynamic **components zones**: rockface, upper channelized erosive debris flow channel, widened dispersive debris flow channel, and outlet. The orange **dotted** line delimits the 378,642 m<sup>2</sup> impacted by the cliff fall studied in this contribution. b) Dust cloud over the southwest slope produced by the 2007 rockfall event (DAV, 2017) b) southeastern slope with remnant dust cloud from the 2016 rockfall event at the southwest slope (DAV, 2016).

185

### 3. Methods

#### 3.1 Multi-temporal quantification of surface change

We used large format aerial imagery surveyed by the Austrian and German Cartographic Survey offices (BEV & LDBV) and by 3D RealityMaps GmbH to investigate the spatial and temporal sediment production, transport, and accumulation patterns of the southwest slope of the Hochvogel in 6 intervals over ten years. All seven surveys (09.2010, 08.2012, 09.2014, 06.2015, 08.2017, 09.2018, and 08.2020) have a nominal 20 cm spatial resolution (supplementary Table 1.) for the production of the digital surface models (DSM) and true orthophotos from the photogrammetric point clouds. The produced DSMs were aligned to the reference dataset acquired on 21.09.2018 by means of a 3D coregistration for the further application of change detection and volume calculation.

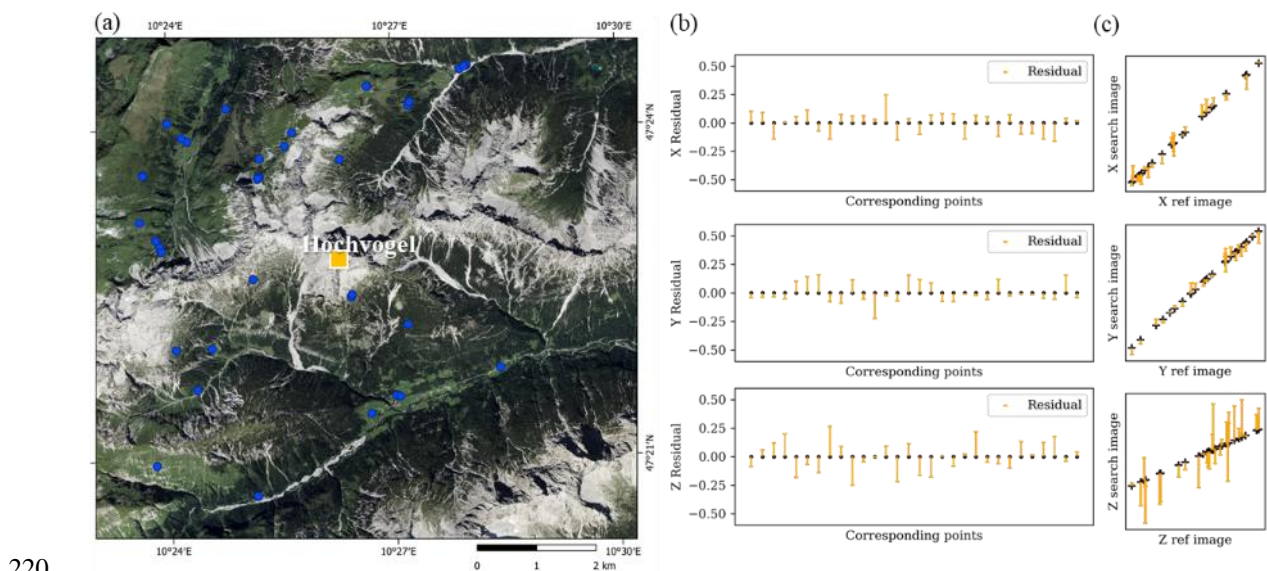
195

### 3.1.1 2.5D topographic time series

The photogrammetric workflow to generate DSM and true orthophoto from nadir view aircraft photographs consist of the initial standardization of the aerotriangulation provided by the survey agencies into the same spatial reference system using the software Inpho and Match-AT by Trimble, and followed by the generation of oriented point clouds, DSM, and orthophotos using the semi-global matching algorithm first developed by (Hirschmüller, 2008) and implemented in the software SURE from nFrames (ESRI) (Haala and Rothermel, 2012; Rothermel et al., 2012). The DSM follows the same grid from the orthophoto, but only high-quality elevation points identified by a multi-triangulation of at least 3 photographs are written in the non-interpolated DSM. We optimized the orthophotos and non-interpolated DSMs for a more precise volumetric calculation in steep terrain by the application of a 7-parameter 3D similarity transformation described by (Eq. (1)). To minimize the 3D distance between a reference surface-dataset (DSM and Orthophoto) (21.09.2018) and the interest datasets, we manually selected 30 multi-temporal well-distributed 3D corresponding points  $(x, y, z)$  located in stable, non-changeable areas using the true orthophotos and the corresponding DSMs, and solved Eq. (1) using the least-squares adjustment solution in python:-

$$210 \begin{bmatrix} x_{obs} \\ y_{obs} \\ z_{obs} \end{bmatrix} = \lambda \begin{bmatrix} \cos(\varphi)\cos(\kappa) & \sin(\omega)\sin(\varphi)\cos(\kappa) - \cos(\omega)\sin(\kappa) & \cos(\omega)\sin(\varphi)\cos(\kappa) + \sin(\omega)\sin(\kappa) \\ \cos(\varphi)\sin(\kappa) & s \in (\omega)\sin(\varphi)\sin(\kappa) + \cos(\omega)\cos(\kappa) & \cos(\omega)\sin(\varphi)\sin(\kappa) + \sin(\omega)\cos(\kappa) \\ -\sin(\varphi) & s \in (\omega)\cos(\varphi) & \cos(\omega)\cos(\varphi) \end{bmatrix} \begin{bmatrix} x_{ref} - x_0 \\ y_{ref} - y_0 \\ z_{ref} - z_0 \end{bmatrix} - (1)$$

where  $[x_{obs}, y_{obs}, z_{obs}]^T$  and  $[x_{ref}, y_{ref}, z_{ref}]^T$  are the vectors of coordinates of the corresponding points at the search-interest surface-dataset  $s(x, y, z)$  and reference surface-dataset  $r(x, y, z)$  with size  $(1, 3 * n_{corresponding\ points})$  respectively ;  $\lambda$  is the uniform scale factor;  $[x_0, y_0, z_0]^T$  is the vector of approximate values of the parameters; and  $\omega, \varphi, \kappa$  represent the rotation Euler Angles used to calculate the orthogonal rotation matrix  $M$ ,  $m_{ij} = M(\omega, \varphi, \kappa)$ . Parameters  $\lambda$  and  $[x_0, y_0, z_0]^T$  are initially approximated to 0 and  $M(\omega, \varphi, \kappa)$  to  $\frac{\pi}{180}$ . The evaluation of the estimated parameters  $M(\omega, \varphi, \kappa)$ ,  $\lambda$  and  $[x_0, y_0, z_0]^T$  after the convergence of the model (5 iterations) results in the elimination of outliers and the warranty of randomness in the residual values defined as the difference between the  $r(x, y, z)$  and  $-s_{trans}(x, y, z)$ , being  $s_{trans}$  the new coordinates of the corresponding points at the search surface after the application of the transformation parameters (Figure 2).



220

Figure 2. a) True orthophoto of the reference surface acquired on 21.09.2018. Blue dots indicated the corresponding points with the search surface acquired on 07.08.2017. Similar spatial distribution is followed for the remaining datasets

225 according to the extent of the acquisition. b) Residuals calculated as the difference between the  $r(x,y,z)$  and  $s_{trans}(x,y,z)$ , being  $s_{trans}$  the new coordinates of the corresponding points at the search surface after the application of the transformation parameters for each spatial axis x, y, and z. c) Spatial distribution of the corresponding points at each spatial axis x, y, and z.

Repetitive topographic surveys, in our case DSMs, allow the identification and quantification of geomorphic changes such as erosion and deposition. We followed the guidelines given by James et al. (2012) and Wheaton et al. (2010) (James et al., 2012; Wheaton et al., 2010) for the estimation of ~~We estimated the~~ area and volume of  
230 change based on 2.5D data, i.e., rasterized topography following Eq. (2):

$$DoD = Z_{new} - Z_{old} \quad (1)$$

where DoD is the difference of elevation between consecutive DSMs ( $Z_{new}$  and  $Z_{old}$ ). Despite the limited  
235 depiction of vertical walls and possible artifacts for overhanging walls, gridded datasets, i.e., DEM, support the fast and straightforward calculation of 2.5 D volumes by Eq. (3):

$$V = a \sum_{i=1}^n DoD_i \quad (3)$$

$$\text{where } a = n * a_{pixel} \quad (4)$$

and  $n$  is the number of pixels conceding with a meaningful change, i.e., pixels over or under a critical threshold,  
240  $a_{pixel}$  corresponds to  $0.4 \text{ m}^2$ , and  $DoD_i$  is the elevation difference between time periods.

We used the non-interpolated DSMs to minimize the change to noise ratio (Wheaton et al., 2010; Anderson, 2019). Elevation uncertainty of photogrammetric surveys is roughly assessed as three times the spatial resolution, however, lighting conditions, surface roughness, and camera configuration among others, imprint an  
245 inhomogeneous spatially distributed uncertainty ~~which estimation remains challenging~~ that remains challenging to estimate. Thus, we evaluated the elevation uncertainty of the elevation change ( $\delta_{DoD}$ ) uncertainty after the 3D-coregistration using 30 independent well-distributed points on stable areas with complex topography for each DoD independently (supplementary Table 2). The uncertainty of the elevation change ( $\delta_{DoD}$ ) elevation uncertainty is, measured as the Root mean square error (RMSE) of the elevation difference in stable areas with complex  
250 topography and, ranges between 30 to 40 cm (supplementary Table 3). We segmented the study area into four regions based on morphometric characteristics, to acknowledge the role of topography on elevation uncertainty. Hereby slope angle and slope aspect, influence the minimum detectable change through time but also imprint morphodynamic characteristics (Sect. 2.). Conservative critical thresholds above the measured coregistration error and elevation uncertainty for each region were determined by best practice between 0.2 to 1 m (supplementary  
255 Table 4 and 5). Note that the critical thresholds certainly influence the calculations of the magnitude of rockfalls, and sediment erosion, transport, and deposition, but will not alter the general conclusions on the rockfalls patterns at the slopes that constitute the summit and the sediment dynamic response to the input of sediment from the cliff fall in terms of reaction and relaxation times.

260 We filter the different sources of topographic changes by semi-automatic filtering, and final manual inspection using 3D visualization. The filtering processes focus on the identification of 'false' rockfalls, defined as over-elongated polygons in the z component in relation to their horizontal area generated due to poor edge depiction. First, we segmented ~~are based on the segmentation of~~ the DoD using a 3x3 circular kernel on a binary mask of



change (1)-no change (0) defined by the critical thresholds. The size of the kernel was selected to segment an  
 265 approximate connected change of a minimum of 1 m<sup>2</sup>. We used descriptive statistical information from each  
 polygon: minimum and maximum elevation change, area of change, volume of change, and mean slope before  
 the change, to filter the polygons using the criteria described in Table 1. The slopes at the Hochvogel are mostly  
 highly-fractured and horizontally layer, thus, rock falls preferentially follow a pseudo-cubic form. ~~Hence, the  
 filtering approach focuses on the identification of changes that are over-elongated in the z-component in relation  
 270 to their horizontal area (area/maximum elevation change <1). These types of changes are identified as “false”  
 rock falls.~~ A 3D visualization supports the final visual inspection.

275

**Table 1. Attributes, argumentation, and threshold value used to filter the change polygons from noise. Threshold values are selected by visual inspection of the filtering results. (A) rockface, (B) Upper channelized erosive debris flow channel, (C) Widened dispersive debris flow channel, and (D) outlet.**

| Attribute                     | Usage   | Threshold value   |
|-------------------------------|---|---|
| Area/Maximum elevation change | Detection and elimination of vertical changes that correspond to poor edge depiction.       | < 1   |
| Mean slope before the change  | Differentiation of erosion and deposition area based on physical parameters.                | Erosion at (A) and (B) is limited to slopes with > 30°<br>Erosion at (C) occurred on slopes > 5°<br><br>Deposition at (A), (B) and (C) is limited by the repose angle of calcareous materials approximated to < 50° |
| Number of pixels of change    | Detection of small changes which are prone to higher uncertainty and visually inconclusive. | ⊆ 15 connected pixels   |

280 The 3D-coregistration process suggest a neglectable horizontal error at the pixel level, thus, the total volume  
 uncertainty ( $\delta V$ ) from Eq (3) is the sum of the uncertainty of each cell of volume ( $\delta v$ ). The cell of volume  $v$  is  
 calculated such Eq (5)-:

$$v = a_{pixel} D o D_{pixel} \quad (5)$$

To propagate the errors of each cell of volume, the partial derivative of Eq (5) with respect to the elevation change,  
 285 which is the variable that has uncertainty, is calculated:

$$\delta v = |v'(D o D)| \delta_{D o D} \quad (6)$$

$$\text{-where - } \delta_{D o D} = RMSE_{Z_{time\ period}}$$

Finally, the volume uncertainty over area A is given by Eq. (7):

$$\delta V = A \delta v \quad (7)$$

290

The proposed workflow for the calculation of volumes of changes in steep terrain using large format high-resolution aerial imagery results from the combination of previously published methodologies and the implementation of intermediate steps that responds to the particularities of the datasets. A summary of the methodological step is presented in Figure 1 supplementary material. Further research is needed to better determine the significant change and the uncertainty on the volume calculation of erosion and deposition in areas with steep and inhomogeneous terrain.

### 3.1.2 Frequency-magnitude curves

A frequency-magnitude curve relates the magnitude of a variable to the frequency of occurrence (Riggs, 1968). The curve is an estimate of the incremental yearly cumulative frequencies from the largest magnitude event to the smallest (Hung et al., 2008). We included both primary and secondary rockfalls in our analysis. We acknowledge the occurrence of coalescent events, given the (multi-) yearly temporal resolution of the datasets (Williams et al., 2019), however, we do not intend to resolve single rockfalls but we aim to decipher the relative rockfall activity in the last decade for each of the rockface slopes that constitute the summit. ~~The frequency analysis aims to compare the activity and relative size distribution~~ (Dussauge-Peisser et al., 2002; Benjamin et al., 2020; Hantz et al., 2021) ~~(Dussauge-Peisser et al., 2002; Benjamin et al., 2020; Hantz et al., 2021).~~ ~~of the different rock face slopes that constitute the Hochvogel summit.~~ We assessed the volumetric errors due to the steep topography by the iterative calculation of the volume of a known event (2016 cliff fall) using all possible combinations of DSMs (Table 6 supplementary material).

### 3.1.3 Cascading geomorphic sediment budgets

A sediment budget describes the input, transport, storage, and export of sediment in a geomorphic system. This concept provides an effective basis for representing the key components of the sediment delivery system within a catchment and for assembling the necessary data to elucidate, understand and predict catchment sediment delivery (Walling and Collins, 2008) and estimate related natural hazards. The geomorphic sediment budget (Wheaton et al., 2010) is calculated as the sum of the masked DoD values of erosion (negative change) and deposition (positive change).

We calculate the proportion of net erosion and net deposition per year ( $\text{m}^3 \text{y}^{-1}$ ) based on the number of days between acquisitions, comparable to previous studies. Conversion to mass (t) is based on reported densities of limestone  $2.6 \text{ t m}^{-3}$  and limestone deposits  $2 \text{ t m}^{-3}$  according to (Krautblatter et al., 2012). Spatially averaged short-term wall retreat rates were calculated by dividing the total rockfall volume per year ( $\text{m}^3 \text{y}^{-1}$ ) by the area over which the volumes were calculated., i.e., northern slope ( $253,643 \text{ m}^2$ ), western slope ( $115,098 \text{ m}^2$ ), southwestern slope ( $254,686 \text{ m}^2$ ), southeaster slope ( $165,037 \text{ m}^2$ ), rockface ( $234,329 \text{ m}^3$ ), upper channelized erosive debris flow channel ( $53,072 \text{ m}^3$ ), widened dispersive debris flow channel ( $91,241 \text{ m}^3$ ) and outlet ( $34,004 \text{ m}^3$ ).

## 3.2. Volume estimation of the 2016 multi-event

### 3.2.1. 3D cumulative volume

The 2016 rockfall dramatically changed the morphology of the southwestern slope of the Hochvogel. A visual  
330 comparison of images taken by Land Tirol during a helicopter flight inspection to the summit on 03.07.2015 and  
the UAV images acquired by the landslide group (Andreas Dietrich) at the Technical University of Munich (TUM)  
using a UAV DGI Phantom 4 during a monitoring survey as part of the AlpSenseBench project on 28.09.2017,  
revealed the pre-event topography of the southwestern slope (Figure 3). Recent developments in dense matching  
algorithms in combination with structure from motion (SfM) retrieve dense point clouds (Eltner and Sofia, 2020).  
335 For a more precise reconstruction of 3D geometry of the cliff fall, particularly on the vertical slopes, we calculated  
the volume of change using the most complete photogrammetric point clouds from an acquisition before the event,  
23.09.2014, and after the event, 07.08.2017. We manually delimited the extent of the 2016 rockfall event based  
on the cloud-to-cloud distance algorithm in [CloudCompare v2.0](#)~~CloudCompare v2.0~~. The volume calculation was  
performed over a grid of 0.2 cm and an average height cell in [CloudCompare v2.0](#)~~CloudCompare v2.0~~. For  
340 visualization purposes, we reconstructed the detached surface by creating a mesh using the Poisson Surface  
Reconstruction plugin (Kazhdan et al., 2020) and the two-point clouds. The approximate orientation of fractures  
was extracted from the photogrammetric point cloud 23.09.2014 using the CloudCompare plugin ~~Compass~~  
(Thiele et al., 2017).

### 3.2.2. Multi-stage detachment analysis

345 For the time interval in which the 2016 failure occurred (July 9 to 11), we downloaded all available seismic data  
from seven surrounding broadband stations (distance to Hochvogel: 12-55 km) (supplementary table 7). By  
analyzing the local seismic amplitude and the corresponding spectrograms at each station, we identified all seismic  
events with the strongest impact at the closest station in Oberstdorf. Rock falls produce a seismic impact over all  
frequencies between 5 and 50 Hz (Dietze et al., 2017; Le Roy et al., 2019); in our case, we expect a clear decrease  
350 in seismic intensity with increasing distance of the stations from the Hochvogel and significant arrival time  
differences of up to 20 s (~~supplementary Figure: 43 supplementary material~~). On the contrary, earthquakes often  
show distinct arrivals of P and S waves, a lower frequency content, and smaller arrival time differences. Local  
anthropogenic noise is characterized by higher frequency contents and missing coincidence of the signal between  
different stations. Following these criteria, we identified all potential seismic signals originating from the rock fall  
355 series at the Hochvogel.

Despite significant variability in the scaling of  $E_p$  to  $E_s$  (cf. (Hibert et al., 2011), [Le Roy et al. \(2019\)](#)~~Le Roy et al., 2019~~ determined a relation between generated seismic energy  $E_s$  and the potential energy of a rock fall  $E_p$   
such:

$$360 \quad E_s = 10^{-8} \times E_p^{1.55} \quad (11)$$

The initially failed volume can then be derived from the potential energy if we determine the fall height of the  
block that generated the seismic signal. We estimated the fall height of the rock fall event from the  
photogrammetric point cloud differences and 3D models. A simple toppling of the center of gravity towards the  
slope corresponds to a fall height of 50-60 m while a sliding of the failed block suggests a probable fall height of

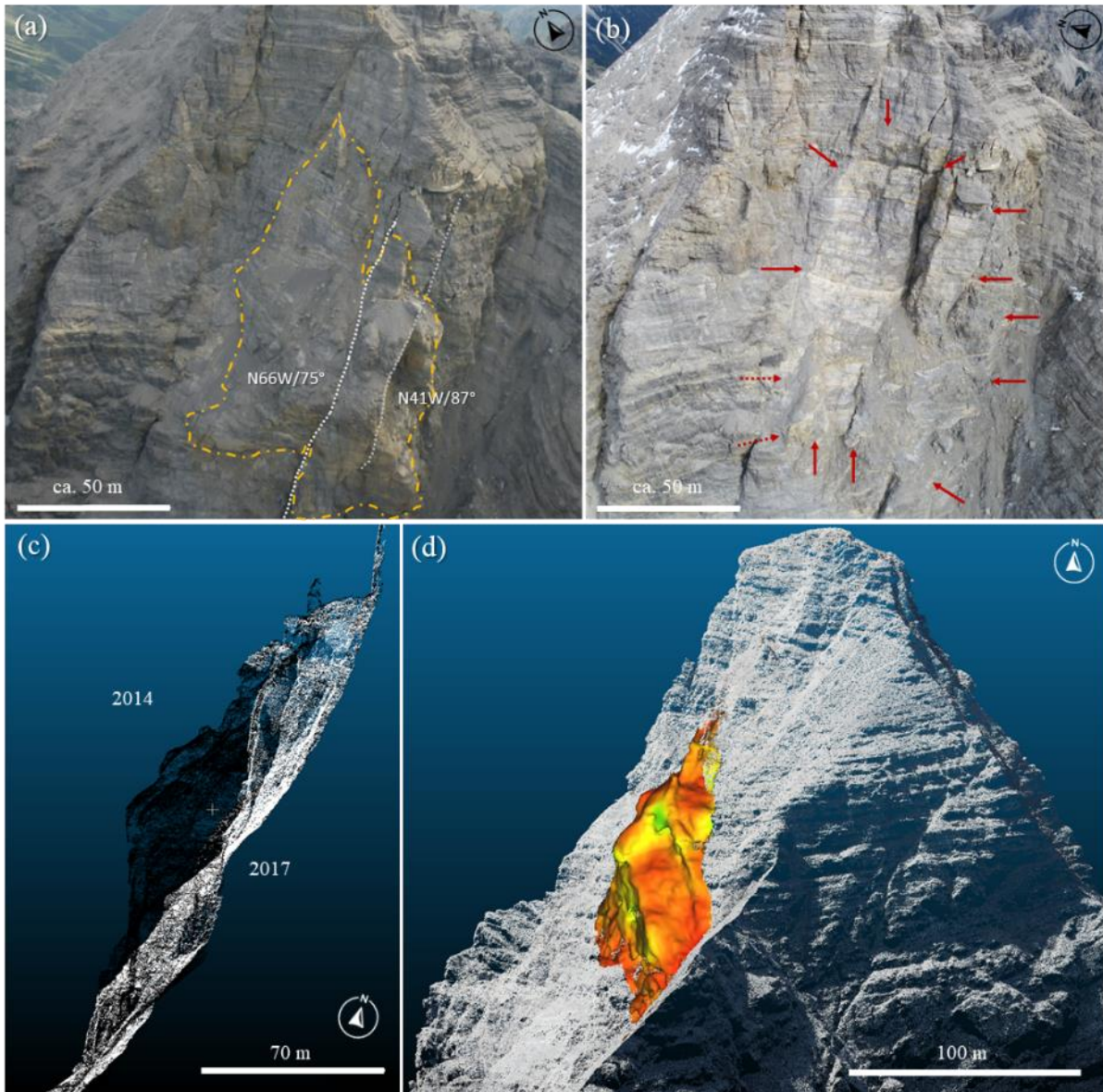
365 75 to 100 m. The calculation of the seismic energy and the determination of all needed parameters mainly follows  
the methodology in [Le Roy et al. \(2019\)](#)~~Le Roy et al., 2019~~ (supplementary Sec. 2). We estimated the error of the  
calculations based on Monte Carlo simulations with 1000 iterations and the variability of the different stations.

#### 4. Results

##### 370 4.1 Multi-stage occurrence of the 2016 cliff fall event

The cliff fall that occurred during the summer of 2016 resulted in the detachment of  $1.31 (\pm 0.01) * 10^5 \text{ m}^3$  of  
dolomite following a multi-stage development. The extent of the cliff detachment is indicated by the clearer color  
tone on the rock surface ([Figure 3b.](#)), and the detachment area was measured to be  $4,777 \text{ m}^2$  using a combination  
of [the best](#) photogrammetric derived point clouds before and after the cliff fall. Prior to the cliff fall, the area was  
375 characterized by a vertical rock tower surrounded by pervasive fractures with orientation NW and pseudo-vertical  
dip angles that may have contributed to the multi-stage detachment by widening preexisting rock discontinuities  
([Figure 3a](#)). The rock tower had a height exceeding 60 meters and was a prominent feature in the landscape.  
Currently, partially disconnected blocks are limited by penetrative fractures and represent areas of potential  
detachments. The cliff fall resulted in a significant change in the morphology of the southwest slope increasing  
380 the mean slope by  $1^\circ$  from  $45.6^\circ$  to  $46.6^\circ$ .



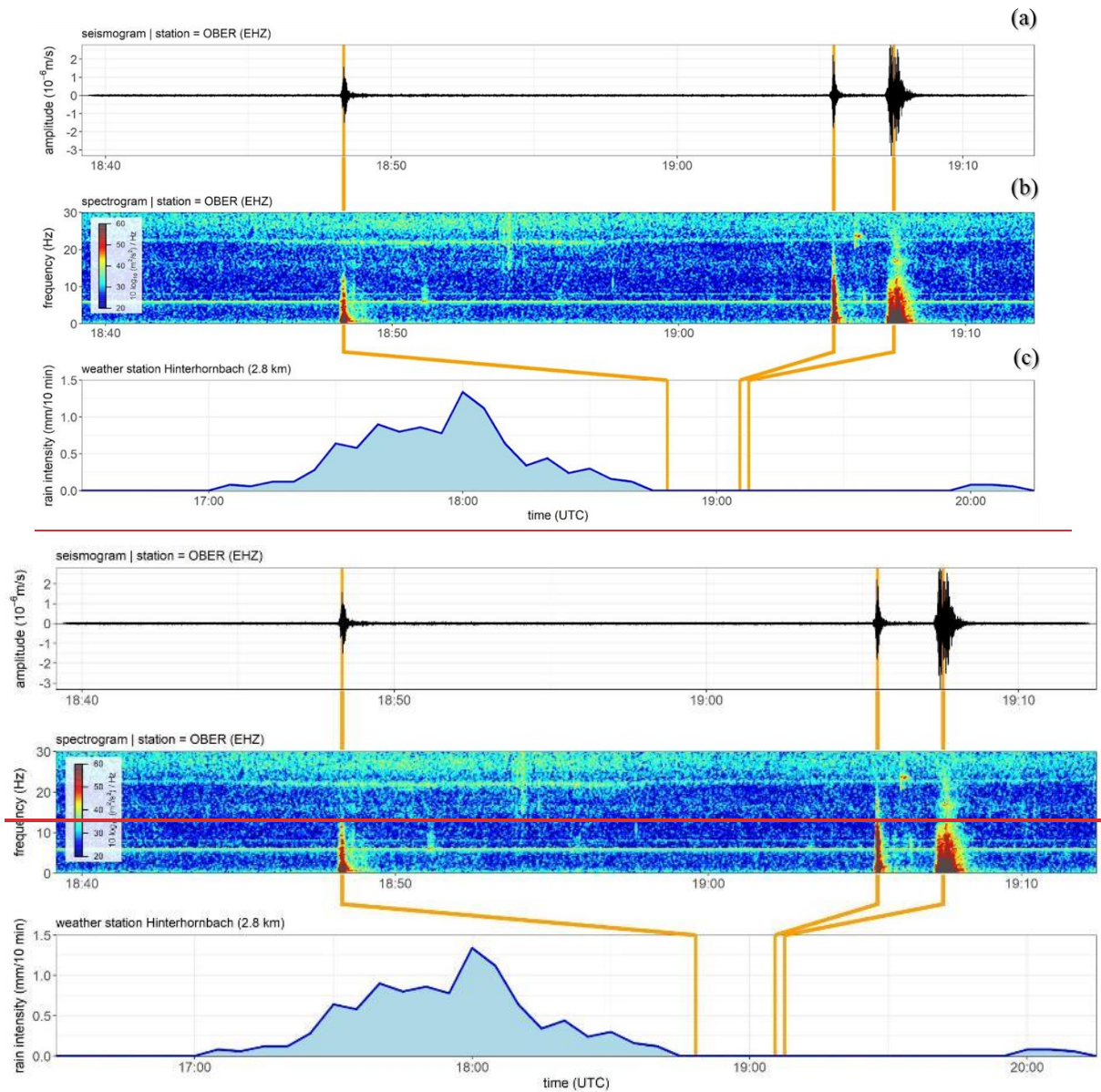


385 **Figure 3.** Picture taken by Land Tyrol before the cliff fall (03.07.2015). The yellow line indicates the cliff fall detachment area in the summer of 2016. The fracture orientations (in white) intend to exemplify approximate structure orientation and must be taken with caution due to the low point density in the exposed fracture surfaces. b) Picture taken by TUM Landslides group (Andreas Dietrich) after the cliff fall (28.09.2017). The red arrows indicates the cliff fall detachment area in the summer of 2016 c) Photogrammetric point clouds from the surveys on 23.09.2014 in black and 07.08.2017 in white. d) Mesh reconstruction of the cliff fall.

The seismic signal analysis indicates a progressive failure of the total mass in at least three to six portions within 3 days (Table 2). The biggest parts of the rock mass failed on the last day (2016.07.11) at 20:48, 21:05, and 21:07  
 390 local time. The volume estimation from the seismic energy at the closest station in Oberstdorf (OBER) results in a median volume of  $1.02 (\pm 0.09) \cdot 10^5 \text{ m}^3$  for a fall height of 60 m. The estimated volume excludes smaller rockfalls, since the limited energy released by these events may not be recorded by the seismic stations. As a result, the seismically estimated volume may underestimate the total amount of material detached.

395 **Table 2. Temporal multiphase cliff fall detachment between July 9th and 11th 2016 at the Oberstdorf station (OBER). Detected event phases and partial volumes (given as median  $\pm$  sd).**

| <b>Event</b> | <b>First arrival time at OBER<br/>in UTC</b> | <b>Status</b>             | <b>Mean volume from station OBER<br/>with fall height = 60 m [m<sup>3</sup>]</b> |
|--------------|--|---------------------------|--|
| 1            | 2016-07-09 08:37:45                          | probably rock fall signal | 8.92 ( $\pm$ 1.52) *10 <sup>3</sup>  |
| 2            | 2016-07-09 17:39:27                          | probably rock fall signal | 1.96 ( $\pm$ 0.32) *10 <sup>3</sup>  |
| 3            | 2016-07-11 17:39:36                          | probably rock fall signal | 2.83 ( $\pm$ 0.54) *10 <sup>3</sup>  |
| 4            | 2016-07-11 18:48:13                          | clearly rock fall signal  | 1.74 ( $\pm$ 0.30) *10 <sup>4</sup>  |
| 5            | 2016-07-11 19:05:19                          | clearly rock fall signal  | 1.83 ( $\pm$ 0.32) *10 <sup>4</sup>  |
| 6            | 2016-07-11 19:07:16                          | clearly rock fall signal  | 5.25 ( $\pm$ 0.88) *10 <sup>4</sup>  |
| SUM          |  |                           | 1.02 ( $\pm$ 0.09) *10 <sup>5</sup>  |



400 **Figure 4. Unmistakable rock detachments on 11th July at the Oberstdorf seismic station (OBER) a) Amplitude of the seismic signal b) spectrogram covering all frequencies up to 30 Hz. c) rainfall intensity at Hinterhornbach (mm/10 min) before and after the rock detachments.**

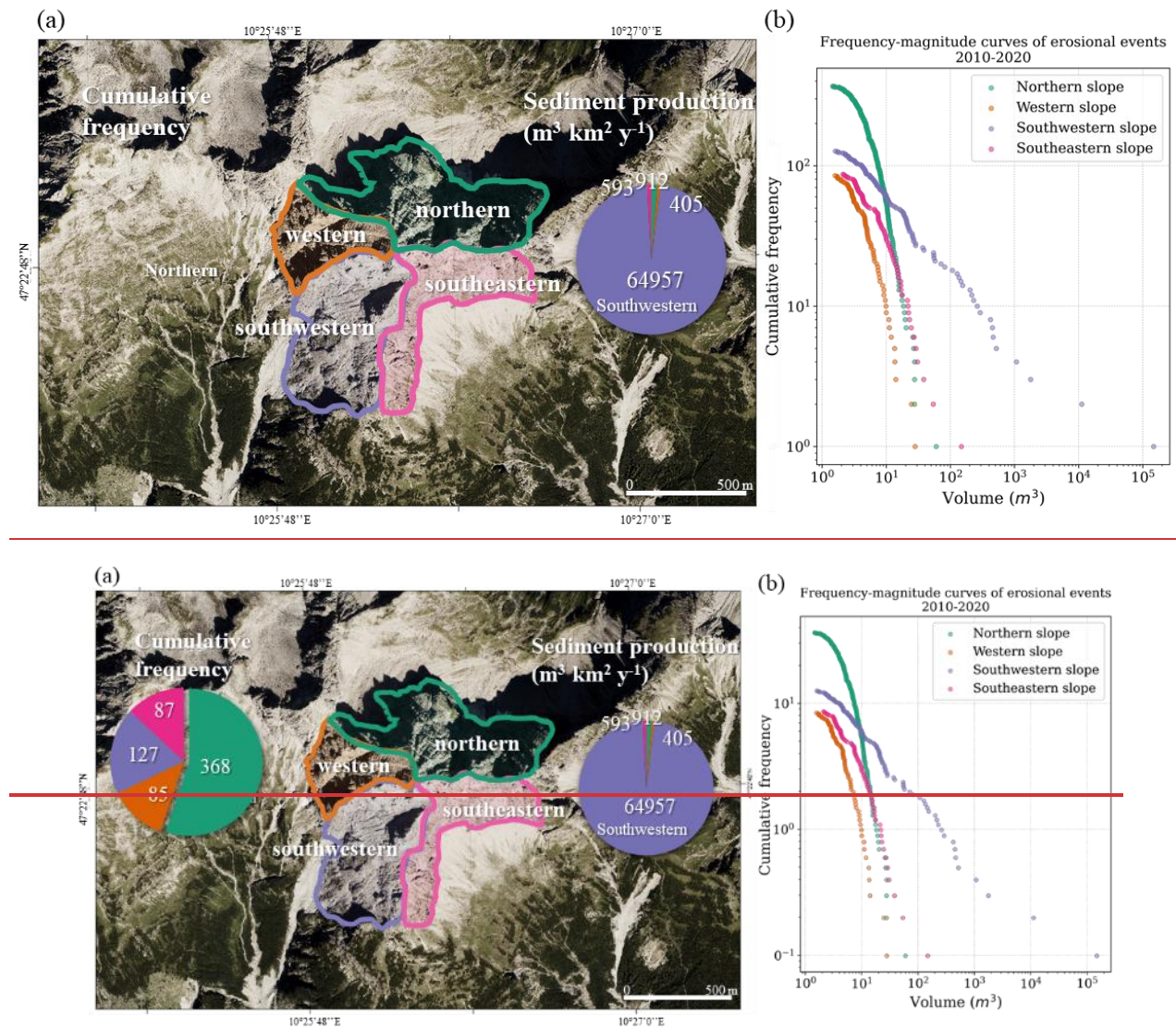
#### 4.2 Summit slope erosion

Over the last decade, the Hochvogel summit has produced  $1.713 (\pm 0.04) \cdot 10^5 \text{ m}^3$  of sediment, corresponding to  
 405 an annual production rate of  $43,990 (\pm 1\,069) \text{ t y}^{-1}$  when assuming a rock density of  $2\,600 \text{ kg m}^{-3}$  (Krautblatter et al., 2012). Notably, 97% of this sediment can be attributed to the 2016 cliff fall at the Southwestern slope. A total of 667 erosional events, including primary and secondary rockfalls, were detected at the Hochvogel summit, with a median volume ranging between  $4.6$  to  $9.3 \text{ m}^3$ . The minimum detectable rockfall volume ranged between  $1.4$  to  $2.1 \text{ m}^3$ , depending on the slope orientation. The sediment production on the four slopes of the summit showed a  
 410 significant disproportion. The western and southeastern slopes had the lowest rockfall frequency, while the northern slope experienced the highest rockfall activity per year (Figure 5). However, when considering the contribution of rockfall magnitudes following the volumetric classification based on Whalley (1974, 1984); Erismann and Abele (2001); Krautblatter et al. (2012), debris falls dominate the northern and western slopes,



while the southeaster slope has a larger proportion of boulder fall, accounting for 55% of the total contribution

415 (Table 3).



420 Figure 5. Erosional events between 2010 and 2020. i.e., primary and secondary rockfalls grouped by slope orientation. a) slope orientation, cumulative frequency per slope, and sediment production per year. b) Frequency-volume Magnitude-Frequency-curves-curves for the 667 erosional events on a logarithmic scale.

Table 3. Contribution of rockfall magnitudes. Volumetric classification based on Whalley, (1974, 1984); Erismann and Abele (2001); Krautblatter et al. (2012). \* Error equal to total volume percentage error of 2.4% (Table 6 supplementary material). Rockwall retreat refers to the horizontal retreat of the vertical rock\_cliff.

|   | northern slope<br>253 643 m <sup>2</sup> |     | western slope<br>115 098 m <sup>2</sup> |     | southwestern slope<br>254 686 m <sup>2</sup> |     | southeastern slope<br>165 037 m <sup>2</sup> |     | Total (m <sup>3</sup> )        |
|---|--|-----|---|-----|--|-----|--|-----|--------------------------------|
|   | Total (m <sup>3</sup> )                  | (%) | Total (m <sup>3</sup> )                 | (%) | Total (m <sup>3</sup> )                      | (%) | Total (m <sup>3</sup> )                      | (%) |                                |
| <b>Debris fall</b><br>Volume < 10 m <sup>3</sup>                    | 1.53 (±0.03) *10 <sup>3</sup>            | 65  | 3.34 (±0.08) *10 <sup>2</sup>           | 71  | 3.37 (±0.08) *10 <sup>2</sup>                | 0   | 3.01 (±0.07) *10 <sup>2</sup>                | 30  | 2.50 (±0.06) *10 <sup>3</sup>  |
| <b>Boulder fall</b><br>10 < Volume < 10 <sup>2</sup> m <sup>3</sup> | 8.11 (±0.20) *10 <sup>2</sup>            | 35  | 1.38 (±0.03) *10 <sup>2</sup>           | 29  | 1.047 (±0.02) *10 <sup>3</sup>               | 1   | 5.41 (±0.13) *10 <sup>2</sup>                | 55  | 2.564 (±0.06) *10 <sup>3</sup> |



|  |                                |                                 |                               |                               |                               |    |                               |    |                                |
|--|--------------------------------|---------------------------------|-------------------------------|-------------------------------|-------------------------------|----|-------------------------------|----|--------------------------------|
| <b>Block fall</b><br>10 <sup>2</sup> < Volume < 10 <sup>4</sup> m <sup>3</sup> | 0                              | 0                               | 0                             | 0                             | 6.57 (±0.16) *10 <sup>3</sup> | 4  | 1.48 (±0.04) *10 <sup>2</sup> | 15 | 6.72 (±0.164) *10 <sup>3</sup> |
| <b>Cliff fall</b><br>10 <sup>4</sup> < Volume < 10 <sup>6</sup> m <sup>3</sup> | 0                              | 0                               | 0                             | 0                             | 1.59 (±0.03) *10 <sup>5</sup> | 95 | 0                             | 0  | 1.59 (±0.03) *10 <sup>5</sup>  |
| <b>Total volume (m<sup>3</sup>)</b>  | 2.34 (±0.053) *10 <sup>3</sup> | 4.72 (±0.0117) *10 <sup>2</sup> | 1.67 (±0.04) *10 <sup>5</sup> | 9.90 (±0.24) *10 <sup>2</sup> | 1.71 (±0.04) *10 <sup>5</sup> |    |                               |    |                                |
| <b>Volume per year (m<sup>3</sup> y<sup>-1</sup>)*</b>                         | 2.31 (±0.06) *10 <sup>2</sup>  | 4.6 (±0.10) *10 <sup>1</sup>    | 1.65 (±0.04) *10 <sup>4</sup> | 9.7 (±0.20) *10 <sup>1</sup>  | 1.69 (±0.04) *10 <sup>4</sup> |    |                               |    |                                |
| <b>Rockwall retreat (mm y<sup>-1</sup>)</b>                                    | <b>0.9</b>                     | <b>0.4</b>                      | <b>64</b>                     | <b>0.5</b>                    |                               |    |                               |    |                                |

425

### 4.3. Geomorphic sediment budget

The short-term denudation rates in the catchment prior to the cliff fall were 45 to 52 mm y<sup>-1</sup>, resulting in a negative catchment sediment budget ranging -1.72-29 (±0.024) \*10<sup>4</sup> m<sup>3</sup> y<sup>-1</sup> and -1.97-59 (±0.044) \*10<sup>4</sup> m<sup>3</sup> y<sup>-1</sup>. Following the cliff fall, the catchment's denudation rates increased abruptly by ten times, reaching 257 mm y<sup>-1</sup>. Despite the erosion of 9.74 (±0.01) \*10<sup>4</sup> m<sup>3</sup> y<sup>-1</sup>, the sediment delivery to the outlet was significantly reduced, resulting in a positive catchment sediment budget of 1.306 (±0.06) \*10<sup>4</sup> m<sup>3</sup> y<sup>-1</sup> (Figure 6a Figure 6). However, two years after the event, within catchment sediment waves dominated the sediment flow to the outlet leading to a negative sediment budget of -1.033 (±0.08) \*10<sup>4</sup> m<sup>3</sup> y<sup>-1</sup>. Subsequently, a slightly positive sediment budget of 6.12 (±2) \*10<sup>2</sup> m<sup>3</sup> y<sup>-1</sup> evidenced the ongoing sediment redistribution within the catchment four years after the cliff fall, even though, the catchment denudation rates returned to pre-event levels of 44 mm y<sup>-1</sup>. Catchment scale erosion and deposition volumes at each time interval are listed in Table 4.

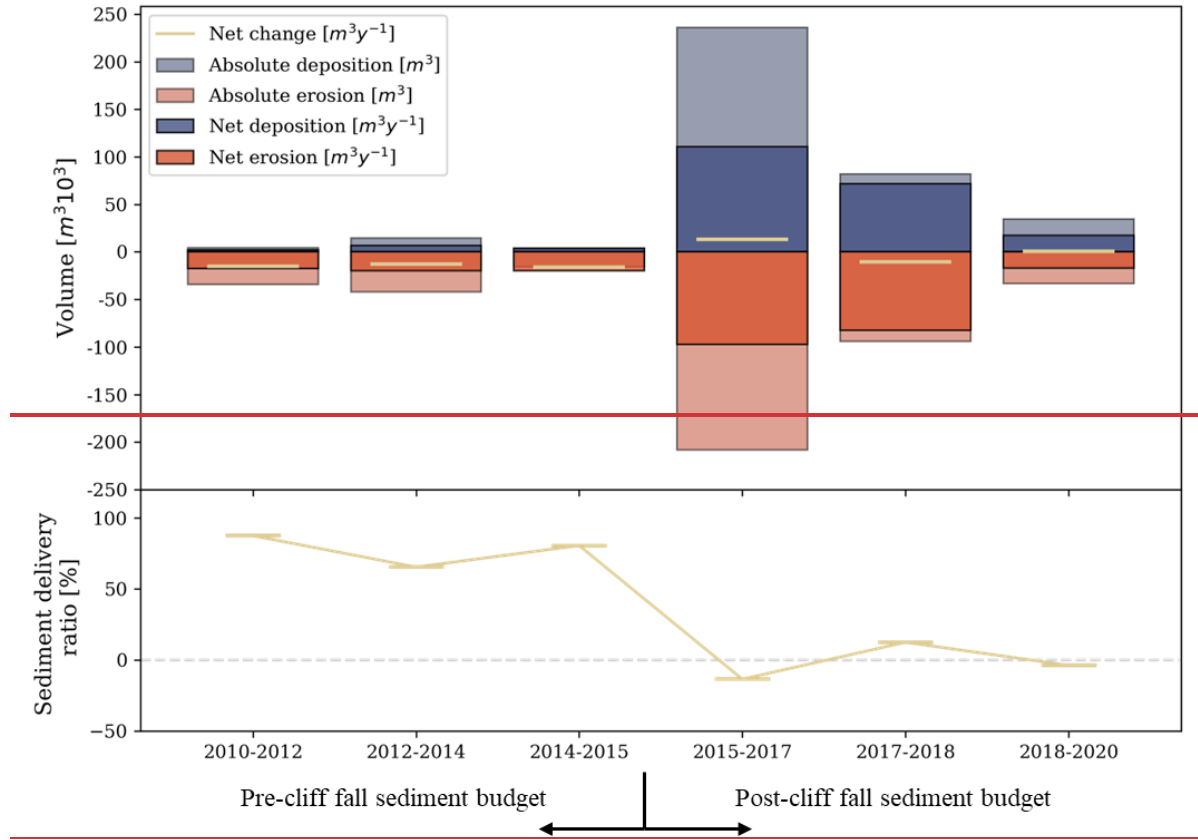


**Figure 6. Time series of geomorphic sediment budgets at the catchment. The bar plot depicts yearly volumes of erosion in red and deposition in blue. The yellow line indicates the net change calculated as the difference between erosion and deposition at each time interval. The estimated uncertainty of the absolute volume is less than 1%, thus, imperceptible due to the scale of the graph. The sediment delivery ratio is expressed as the proportion of sediment leaving the basin and the total net erosion.**

440

**Table 4. Catchment scale erosion, deposition and net volumes ( $m^3$ ). Catchment denudation rates ( $mm\ y^{-1}$ ) were calculated based on the affected area extend ( $378,642\ m^2$ ). The volume uncertainty is calculated independently for each single interval and process, i.e., erosion and deposition. \* Error propagated from erosion and deposition uncertainties (Table 6 supplementary material).**

445

| Interval  | Erosion                      |                        | Deposition                 |                        | Net change                |                           |
|-----------|------------------------------|------------------------|----------------------------|------------------------|---------------------------|---------------------------|
|           | Volume ( $m^3$ )             | Rates ( $mm\ y^{-1}$ ) | Volume ( $m^3$ )           | Rates ( $mm\ y^{-1}$ ) | Volume ( $m^3$ )          | Volume* ( $m^3\ y^{-1}$ ) |
| 2010-2012 | $3.440 (\pm 0.02) * 10^4$    | 45                     | $4.237 (\pm 0.006) * 10^4$ | 5                      | $-2.97 (\pm 0.03) * 10^4$ | $-1.51 (\pm 0.01) * 10^4$ |
| 2012-2014 | $4.20 (\pm 0.02) * 10^4$     | 52                     | $1.45 (\pm 0.01) * 10^4$   | 18                     | $-2.75 (\pm 0.04) * 10^4$ | $-1.29 (\pm 0.02) * 10^4$ |
| 2014-2015 | $14.5429 (\pm 0.032) * 10^4$ | 52                     | $2.998 (\pm 0.002) * 10^4$ | 10                     | $-1.24 (\pm 0.03) * 10^4$ | $-1.59 (\pm 0.04) * 10^4$ |
| 2015-2017 | $2.08 (\pm 0.002) * 10^5$    | 257                    | $2.36 (\pm 0.01) * 10^5$   | 291                    | $2.78 (\pm 0.13) * 10^4$  | $1.30 (\pm 0.06) * 10^4$  |
| 2017-2018 | $9.38 (\pm 0.04) * 10^4$     | 217                    | $8.20 (\pm 0.04) * 10^4$   | 189                    | $-1.18 (\pm 0.09) * 10^4$ | $-1.03 (\pm 0.08) * 10^4$ |
| 2018-2020 | $3.33 (\pm 0.02) * 10^4$     | 44                     | $3.46 (\pm 0.01) * 10^4$   | 46                     | $1.21 (\pm 0.43) * 10^3$  | $6.12 (\pm 2) * 10^2$     |

#### 4.4. Geomorphic sediment budgets across the sediment cascade

The differentiated geomorphic sediment budgets (Figure 6b) and time series of spatial distribution of differences of DSMs (Figure 7) and differentiated geomorphic sediment budgets (Figure 8) reveals the fast system response to the cliff fall. The concept of sediment continuity refers to the transfer or exchange of sediment across various

450

parts of the hillslope system, which involves the conservation of mass among sediment inputs, stores and output (Joyce et al., 2018). Sediment storages and sinks (marked as (1), (2), (3), and (4) in [Figure 7](#)) define the boundaries between different morphodynamic **components/zones**, which are characterized by slight changes in mean slope that imprints morphological controls on transport processes. Regardless of the existence of depositional landforms, sediment continuity dominates from 2010 until 2014 evidenced in negative net change at all the geomorphic system **components/zones**.

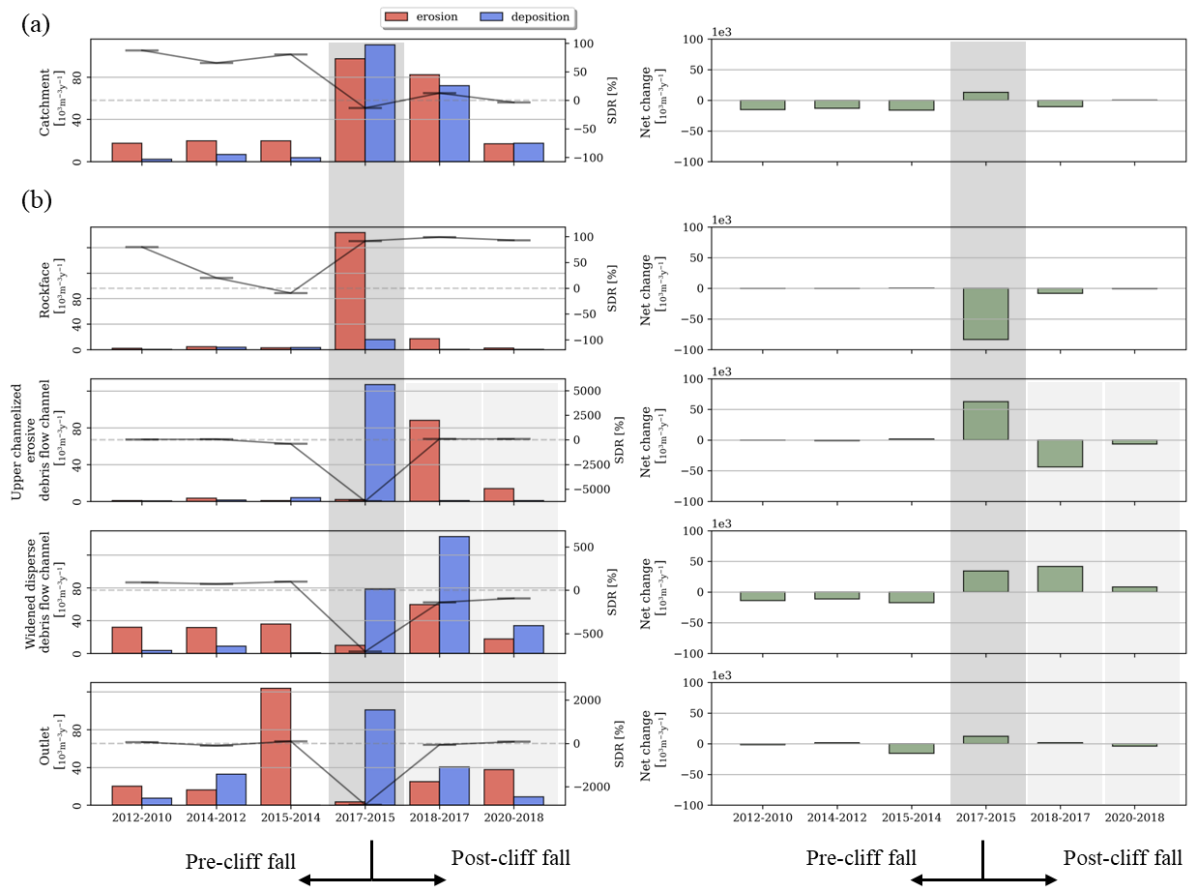


**Figure 6. Time series of geomorphic sediment budgets. a) Geomorphic sediment budgets at the catchment scale. b) segregated sediment budget into the four morphodynamic zones. Left column: The bar plot depicts yearly volumes of erosion in red and deposition in blue (units at the left axis). The black line indicates the sediment delivery ratio expressed as the proportion of sediment leaving the morphodynamic zone from the total net erosion (units at the right axis). Right column: yearly net change calculated as the difference between erosion and deposition. The estimated uncertainty of the absolute volume is less than 2% thus, imperceptible due to the scale of the graph. Dark grey polygons highlight the temporal stamp at which the cliffs fall took place. Lighter grey indicates the system response two and four years after the event. Note how the reverse net changes propagate downslope the system through time.**

An initial disruption in the sediment continuity is observed between 2014 and 2015. At the rockface, boulder and block falls occur, which detach from the sub-vertical wall and deposit at its base. Additionally, in the upper channelized erosive debris flow channel, less than  $< 10^2 \text{ m}^3$  of recently deposited material (less than two years of residence time) are internally redistributed. However, even during this period of localized disruption, sediment redistribution continues to take place at the widened debris flow channel, which ensures sediment delivery to the outlet into the braided sediment-supercharged Jochbach river ([Figure 7](#)).

Following the cliff fall event, there was an immediate disruption of sediment transfer among the different regions of the system, with about 75% of the produced sediment being deposited at the upper channelized erosive debris

flow channel (Figure 6b, 2017-2015). A total of  $1.356 (\pm 0.003) * 10^5 \text{ m}^3$  of sediment were deposited over the 1.5 km length of the upper channelized erosive debris flow channel (Figure 8). Despite the positive sediment budget at the widened disperse debris flow channel, massive deposition occurred at the outlet. The bi-yearly temporal resolution masks the highly dynamic sediment transport, however, t—The formation of a terrace of almost 3 m  
480 evidence the deposition of at least positive net change of  $2.60 (\pm 0.03) * 10^4 \text{ m}^3$  after the cliff fall. Field evidence suggests the infill of the outlet flood plain with new debris that impacted the dynamics of the riverbed (Figure 3 supplementary material). The pre-event channel of the Jochbach river is filled with up to 4 m of material in its deeper part at the end of 2017 (one year after the cliff fall) (Figure 7, morphodynamic zone D). The infill results in a migration of the channel to the center of the Outlet flood plain marked by a discontinuous erosional area in  
485 Figure 7 for 2017-2018, and finally the formation of a main channel towards the north, evident in Figure 7 by the continuous erosional pattern for the time interval between 2018 and 2020.  
Although the stream power was strong enough to incise the terrace and prevent the formation of a dam, the outlet flood plain was filled with new debris that impacted the dynamics of the riverbed.

490 A dramatic inversion from deposition to erosion occurs two years after the cliff fall. Sediment waves or slugs deposited  $8.14 (\pm 0.04) * 10^4 \text{ m}^3$  at the apex of the widened dispersive debris flow channel infilling the valley with 3 m of transported material which increased to almost 10 m four years after the cliff fall (Figure 7 and Figure 9  
supplementary Fig. 2, profile C-C’). Despite the increased sediment input due to the cliff fall, there were reversed net changes between the widened dispersive debris flow channel and outlet four years after the cliff fall (Figure  
495 Figure 76, 2018-2020).

## 5. Discussion

The recently available (multi-) annual high resolution aerial imagery datasets provide an insightful look of  
500 sediment cascades at a decadal scale. Even if the bulk volumes of erosion and deposition register coalesces of rockfall and debris flow events, the temporal resolution reveal patterns of sediment redistribution and geomorphic response time to a disturbance caused by the increased sediment input due to a cliff fall (Owens et al., 2010). Even though the proposed 3D-coregistration workflow optimizes the DSMs extracted from consecutive nadir view large format aerial surveys for volumetric calculations in steep terrain, there are still limitations on the representation  
505 of complex topography. Thus, it requires careful thought about the validity of the measurements. Despite this, the presented results are paramount to identifying and better understanding coupling mechanisms of high-magnitude slope events at a high temporal-spatial resolution to the fluvial system at a catchment scale. The analysis of within hillslope morphodynamics and its coupling with the fluvial system exemplify the alpine catchment response to future climatic changes and landscape dynamics.

### 5.1. Validity of measurements

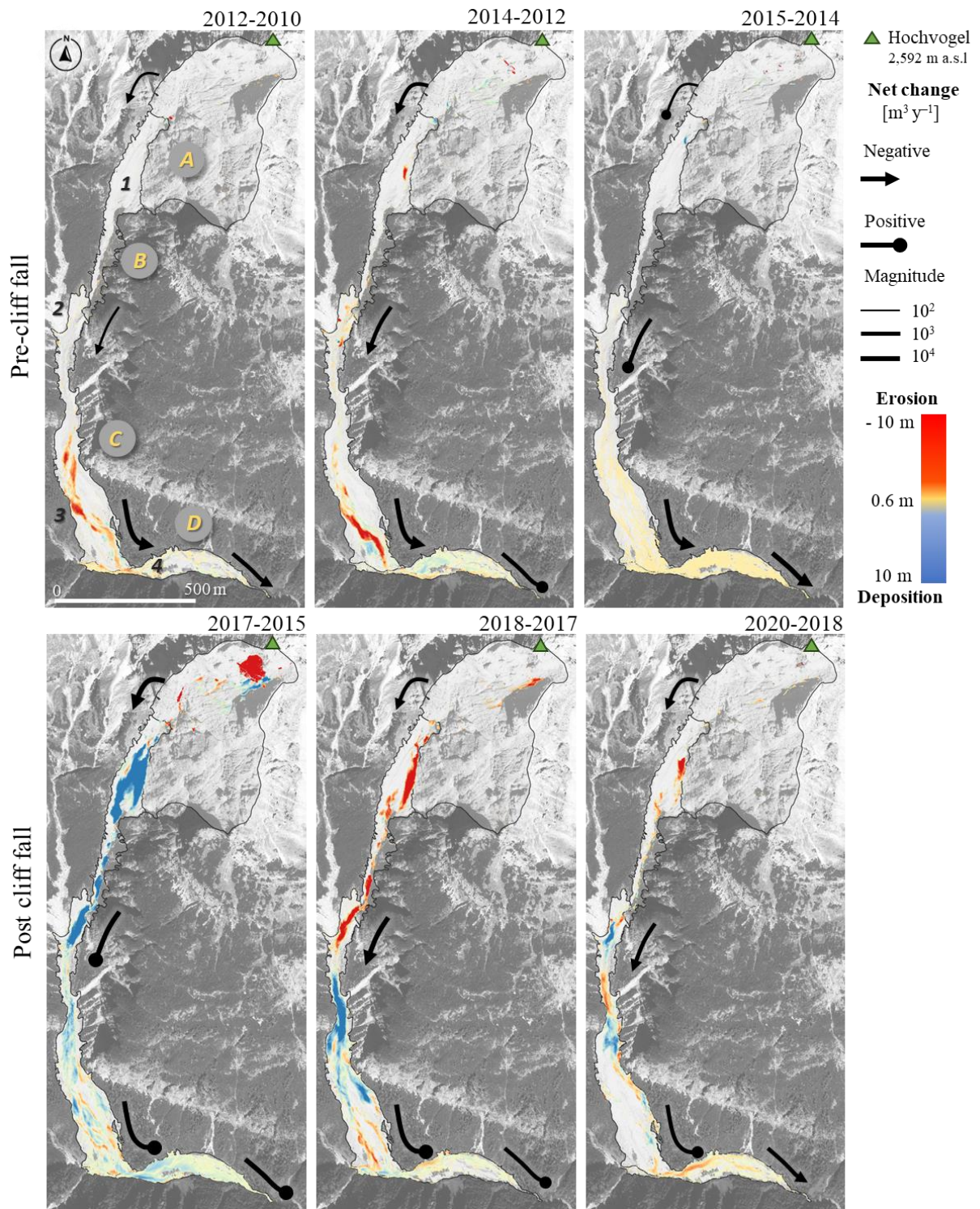
Considering the inhomogeneity of the aerial imagery, the quantitative data described above are comparable to other published results obtained by digital photogrammetry (e.g., (Kaufmann and Ladstädter, 2003; Schiefer and Gilbert, 2007; Marzolf and Poesen, 2009; Fabris and Pesci, 2009; Micheletti et al., 2015; Hilger and Beylich, 2018; Geissler et al., 2021). The authors acknowledge the limitations of aerial imagery to depict vertical surfaces



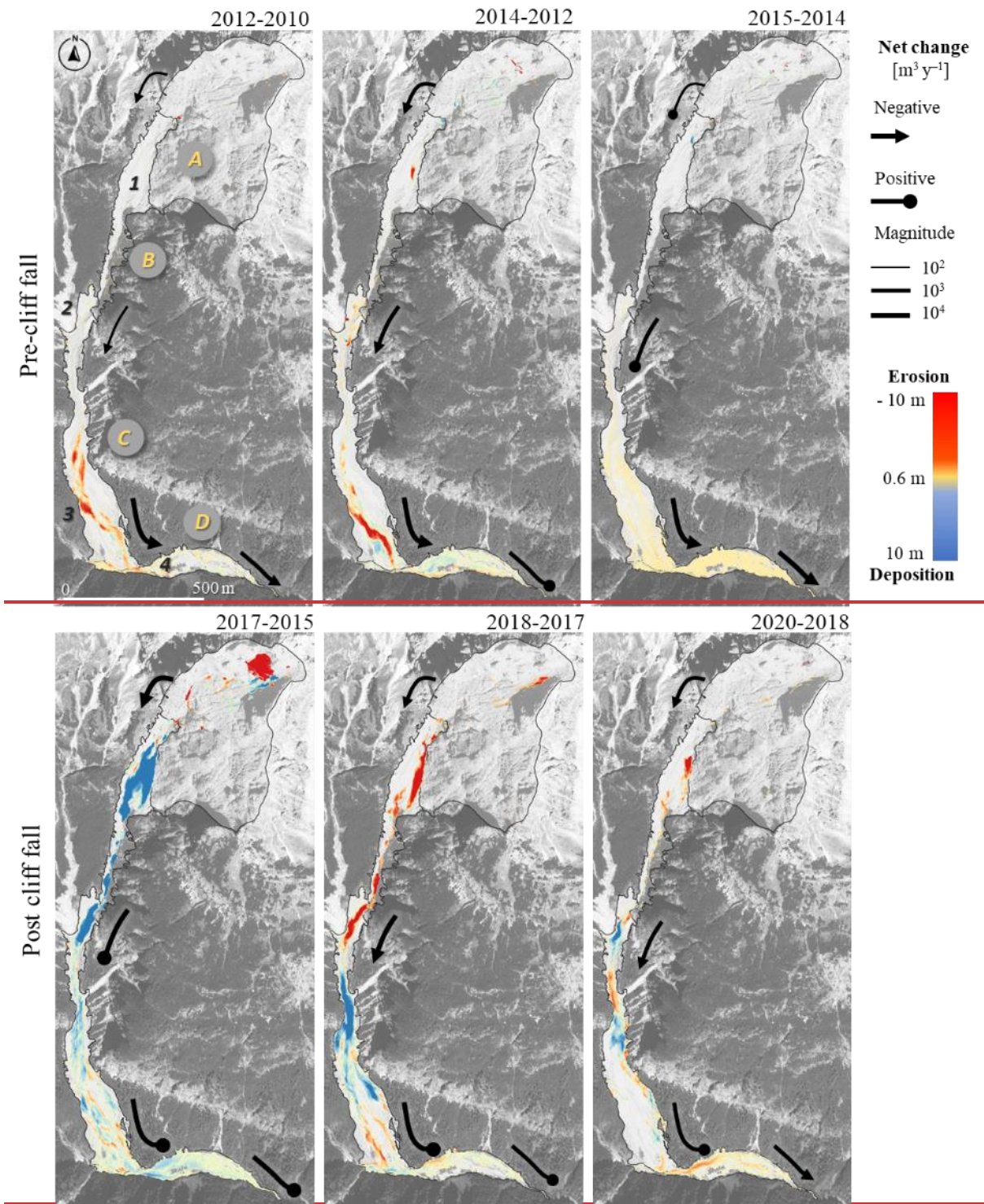
515 and in particular negative vertical surfaces. Nevertheless, the proposed workflow resulted in consistent landscape  
representations through time, evidenced by topographic profiles extracted from the DSM and volume calculation  
of the 2016 cliff fall using all possible DSM combinations (Table 6 supplementary material). Additionally, the  
back calculation of the failed volumes from the seismic signals of regional stations (Sec. 4.1.) is in the range of  
the photogrammetrically determined volumes, thus supporting the results via a second methodological approach.

520

~~This suggest that the sediment transport processes had not fully recovered to pre disturbance levels, even though,  
the sediment continuity within the catchment was restored one year after the initiation of the disturbance, i.e.,  
increased sediment due to the cliff fall.~~







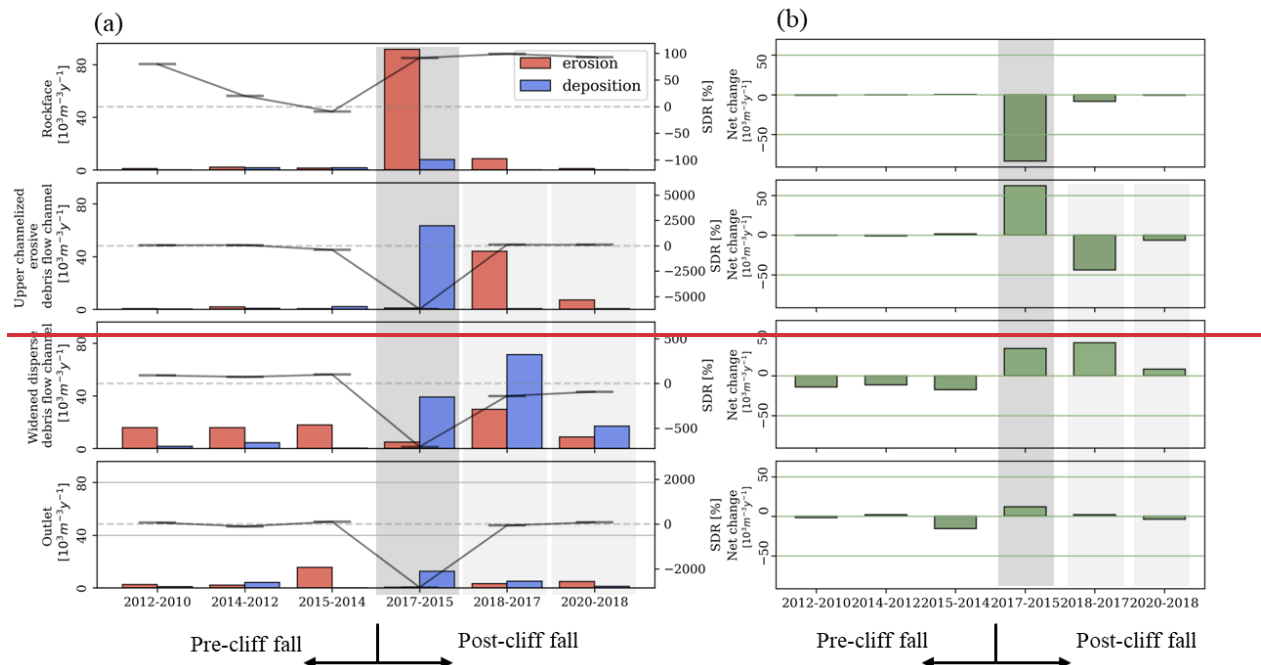
525

Figure 7. Time-series of spatial distribution of erosional (red) and depositional (blue) areas with black arrows as an indication of sediment continuity based on the net changes. (A) rockface (B) upper channelized debris flow channel, (C) widened dispersed debris flow channel, and (D) outlet to the Jochbach river. (1), (2), (3), and (4) mark the position of morphological blockages corresponding to slope changes that promotes deposition thus attenuation in the sediment flux.

530

The braided sediment supercharged Jochbach river incised the 3m terrace formed after the cliff fall by developing a single fluvial channel confined towards the north side of the alluvial plain, opposite to the pre event river channel, located at the south of the alluvial plain. However, a braided channel characterizes the lower outlet sink

535 suggesting an ongoing adjustment to the depleted sediment delivery ratio as a consequence of the cliff fall event.



540 Figure 8. Segregate sediment budget. a) Left axis: Bar plot for net yearly erosion and deposition volumes. Right axis: Sediment delivery ratio. b) net change as an indicator of sediment continuity. Dark grey polygons highlight the temporal stamp at which the cliffs fall took place. Lighter grey indicates the system response two and four years after the event.

## 5. Discussion

545 The scarcity of high-magnitude rockfalls limits the understanding of the physical response of mountain catchment to a sudden increased of sediment input. Digital photogrammetry and image-matching algorithms revolutionized the usage of optical sensors to study topographic changes. The recently available high-resolution temporal and spatial datasets provide a fresh look for geomorphic responses and the time lag between disturbance (increased sediment input due to cliff fall) and reaction (geomorphic response: increased sediment transport by means of debris flows) times from which typically short-term responses become a societal concern (Owens et al., 2010). Even though the proposed 3D-coregistration workflow optimizes the DSMs extracted from consecutive nadir view large format aerial surveys for volumetric calculations in steep terrain, there are still limitations on the representation of complex topography. Thus, it requires careful thought about the validity of the measurements. Despite this, the presented results are paramount to identifying and better understanding coupling mechanisms of high-magnitude slope events at a high temporal spatial resolution to a wide extent. The analysis of within hillslope morphodynamics and its coupling with the fluvial system exemplify the alpine catchment response to future climatic changes and landscape dynamics.

550

555

### 5.1. Validity of measurements

560 Considering the inhomogeneity of the aerial imagery, the quantitative data described above are comparable to other published results obtained by digital photogrammetry (e.g. (Kaufmann and Ladstädter, 2003; Schiefer and Gilbert, 2007; Marzoff and Poesen, 2009; Fabris and Pesci, 2009; Micheletti et al., 2015; Hilger and Beylich, 2018; Geissler et al., 2021)). The authors acknowledge the limitations of aerial imagery to depict vertical surfaces

~~and in particular negative vertical surfaces. Nevertheless, the proposed workflow resulted in consistent landscape representations through time evidenced by topographic profiles extracted from the DSM and volume calculation of the 2016 cliff fall using all possible DSM combinations (supplementary Table 6). Additionally, the back calculation of the failed volumes from the seismic signals of regional stations (Sec. 4.1.) is in the range of the photogrammetrically determined volumes, thus supporting the results via a second methodological approach.~~

565

Even though we followed a very conservative approach, possible overestimations of the volumes are expected, particularly for the rockface where complex topography predominates. When visualizing the point clouds, it is possible to perceive the dense point cloud on the horizontal surfaces, but little to no points on vertical and pseudo-vertical surfaces for some of the datasets (e.g., 2015 dataset). Additionally, even if the vertical sides are completely depicted, the gridded component of the analysis poorly represents the vertical topography. Nevertheless, note that poorly represented areas are excluded from the DSMs used for the calculation of topographic change. On the other hand, the results on the northern slope (Figure 5a), often acquired under poorer illumination conditions, are prone to higher uncertainty. The proposed workflow optimizes the relative uncertainty in the elevation component for each dataset and assesses systematic errors minimized by a spatially uniform critical threshold, but additional research is needed to better estimate the spatial distribution of random errors and proxies that leads to the quantification of a spatially variable uncertainty. ~~On the other hand, the results on the northern slope (Figure 5a), often acquired under poorer illumination conditions, are prone to higher uncertainty.~~ (Wheaton et al., 2010). Therefore, the

570

575

580

~~The 3D coregistration successfully mitigates spatial discrepancies between surveys and evaluate the relative correspondence of x, y and z in the range of the spatial resolution. A remaining challenge lies in the assessment of the ratio to noise. The~~ segmentation approach was designed to filter topographic changes at each landscape compartment ~~having taking~~ into account the stated data limitations. Lower uncertainty is achieved at the widened dispersed debris flow channel and outlet due to more favorable geometry for the photogrammetric reconstruction, i.e., perpendicular surface to the nadir-view which corresponds to a lower slope angle to flat topography. the smoother surfaces favorable for the photogrammetric reconstruction. In spite of the discussed drawbacks, the presented workflow aims for an efficient and fast calculation of volumetric changes foreseen by the usage of aerial imagery for the early detection of future hazardous areas over wide extents or multiple basins in the context of a fast-changing climate and landscape.

585

590

The temporal resolution from large-format digital aerial surveys limits the quantification of single events, thus, the analysis of seismic datasets complements the photogrammetric record by deciphering the coalescence of events. The energy released by the rockfalls associated with the 2016 cliff fall was sufficient to be recorded despite the distance of the seismic stations (the closest station located at 11 km); therefore, we elucidate the multi-stage detachment of possibly 6 events with exact timing (3 block falls followed by 3 cliff falls). Contrary, the energy released by individual debris flows event is considerably less, thus challenging the usage of the current seismic network. Note that ~~The complementary analysis of seismic datasets elucidates the multi-stage detachment of possibly 6 events with exact timing (3 block falls followed by 3 cliff falls).~~ The latest three seismic events identified as rockfalls show clear evidence of a source located close to the Hochvogel rock failure, while the first three events are harder to constrain due to their smaller amplitude (Figure 8a,b and c supplementary material).

595

600



Nevertheless, these also show the same intensity-distance decay and signal arrival time patterns and can therefore be considered. Additionally, the respective sub-event's percentage of the total volume is very similar for the stations OBER, RETA, DAVA, MOTA and A307A (~~supplementary Figure 7 and Table 13 supplementary material 6, Table 13~~). The stations PART and ZUGS must be excluded due to their bad signal-to-noise ratio in the relevant frequency band. For a fall height of 60 m, the volume estimated from the seismic signal at OBER is 20 % lower than that estimated photogrammetrically, but the seismic method neglects detachments that are too small to be recorded by the distant broadband sensor, detachments from the same source area but not belonging to the 3-day event, and energy that gets lost due to fragmentation of the failed mass. The other stations further away underestimate the volume due to stronger signal damping, distortion and worse coupling compared to the closest station OBER.

## 5.2. Rockfall activity as landscape re-shaping mechanism

Bi-annual rockwall retreat rates for the five years prior to the cliff fall, ~~which~~ averaged  $6.5 \text{ mm y}^{-1}$ , slightly exceeding short-term (< 10 years) rock wall retreats for limestones (Draebing et al., 2022). ~~The maximum pre-cliff fall rockwall retreat corresponds to with a maximum retreat of~~  $9.5 \text{ mm y}^{-1}$  between 2012 and 2014. ~~The rockwall retreat rates~~ However, they are consistent with previous ~~finding findings~~ of enhanced rockfall activity for carbonate cliffs (Krautblatter et al., 2012). The (multi-) annual temporal intervals used in this study are unlikely to be sensible to precursory deformations, however, patterns of erosion across the rockface slope in the years prior to the cliff fall might reveal signs of alert. Close-up observations of the area of the cliff failure evidence block fall and boulder fall at the base of the failure with volumes of  $1.71 (\pm 0.005) * 10^3 \text{ m}^3$  and  $1.05 (\pm 0.003) * 10^3 \text{ m}^3$  in 2012-2014 and  $2.91 (\pm 0.01) * 10^2 \text{ m}^3$  in 2014-2015 reflecting a main deformation area (Kromer et al., 2018)(Kromer et al., 2018). The cliff fall resulted in the rockwall retreat of  $390 \text{ mm y}^{-1}$  between 2015 and 2017 increasing the mean steepness of the rockface by 1%. The consecutive detachment of at least 6 blockfalls over 3 days follows an increase in magnitude from  $10^3 \text{ m}^3$  to  $10^4 \text{ m}^3$  previously suggested by other studies (e.g., (Kromer et al., 2017; Rosser et al., 2007; Abellán et al., 2009; Benjamin et al., 2020)(Kromer et al., 2017; Rosser et al., 2007; Abellán et al., 2009; Benjamin et al., 2020), and paramount for the understanding of cascading risk in alpine regions.

~~Despite of the greater distance between the Hochvogel summit and the seismic stations used to characterize the 2016 cliff fall compared to the original source (Roy et al., 2019), the energy released by the 6 sub-events was sufficient to record and discriminate them. Regardless of the high temporal resolution achieved with the seismic analysis compared to the photogrammetric records, t~~The triggering mechanism for this multi-stage event ~~is is~~ hard to constrain ~~and needs further research~~ because of the lack of high-resolution climatic datasets at local scales. Among common rockfall triggering factors are precipitation and cyclic thermal stressing (Dietze et al., 2017b, 2021)(Dietze et al., 2017b). Climatic records from the surrounding of the Hochvogel (Station located at Obersdorf) ~~showed that~~ ~~The~~ multi-stage event is preceded by a phase of several dry and hot summer days. In the night before the first block fall, minor amounts of rain have been recorded, but the three final cliff falls on July 11<sup>th</sup> are preceded by more intense rainfall of up to  $1.4 \text{ mm}/10 \text{ min}$  with a time lag of less than 1 h (Figure 4)(Figure 4c). Also, all recorded events happened during the morning and evening hours where a strong thermal gradient might have an influence on the stressing of the rock mass (Dietze et al., 2017b, 2021)(Dietze et al., 2017b, 2021).

640 Contrary to rockfall observations from high temporal monitoring of cliff evolution (Williams et al., 2019), the sub-events prior to the cliff fall are unlikely to follow a pattern of increasing frequency and volumes through time, and even if rockfalls at the proximity of the 2016 cliff fall are mapped as early as between 2010-2012 and 2012-2014, precursory rockfall behavior and triggering mechanism are beyond of the scope of this study.

### **5.3. Mechanism of sediment delivery continuity under a system disturbance.**

645 Typical geomorphic responses to disturbances include increased rates of sediment remobilization, transport and deposition (e.g., (Owens et al., 2010; Bennett et al., 2013; Baer et al., 2017; Frank et al., 2019; Savi et al., 2023), however, sediment export from the basin rarely reflects changes in sediment transfer within a catchment (Walling, 1983; Walling and Collins, 2008; Burt and Allison, 2010) due to the high variability in time and scale of sediment morphodynamics. The catchment sediment budgets at the Hochvogel clearly suggest a perturbation in the system

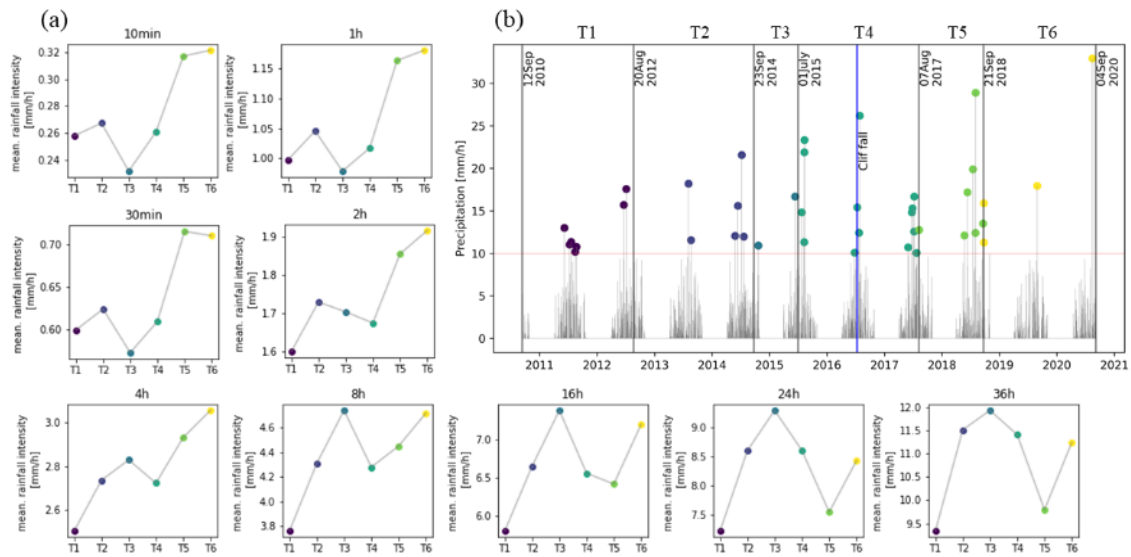
650 with at least a year reaction time evidenced in the shift between predominant deposition to increased erosion. The segregated sediment budget (Figure 6a) and the time series of spatial distribution of erosion and deposition (Figure 7) provide insides on the predominant processes controlling the transfer of sediment within the slope. Conceptual models on sediment cascades on landslide-prone catchments propose the temporal accumulation on slopes from landslide deposits that become available for further remobilization (Harvey, 2001). Sediment transport depends

655 on hydrological conditions and sediment supply, while superimposed debris flows are a common and efficient mechanisms of sediment transport (Benda and Dunne, 1997; Schwab et al., 2008; Bennett et al., 2013; Clapuyt et al., 2019). The surrounding of the Hochvogel displays an increased mean seasonal (April-November) rainfall intensity over the last decades for events with durations of less than 4 hours (Figure 8a); however, the number of days with precipitation exceeding rainfall thresholds reported in the literature for sediment transport (2.2 mm/10

660 min) and debris flows initiation (3.8 to 9.6 mm/10 min and 5 and 15 mm/h) (Hürlimann et al., 2019) exhibit no notorious difference between the periods before and after the cliff fall proving no clear rainfall related apparent trigger for the massive sediment redistribution after the cliff fall. Note the increased number of days with exceeding rainfall thresholds of 10mm/h, 3.8 mm/10min, and 9.6mm/10min for the time interval when the cliff fall occurred (Figure 8b. 2015-2017: T4) while a depositional regime characterizes the sediment dynamics during

665 this period as a consequence of the massive sediment production from the cliff fall. Conversely, the number of days exceeding common rainfall thresholds for the time interval between 2017-2018 (T5 in Figure 8b) characterized by massive sediment redistribution within the catchment is similar to pre-cliff fall intervals. These findings convey with previous studies where no clear rainfall apparent trigger for massive sediment redistribution was found (e.g.,(Bennett et al., 2013; Frank et al., 2019), while, numerical modeling demonstrate that both

670 antecedent moisture and sediment storage are key for debris flow prediction (Bennett et al., 2013, 2014).



675 **Figure 8. Intensity-duration and frequency analysis for a diversity of rainfall events measured at the**  
**precipitation station 6290-Hinterhornbach/AUS. Data basis: Deutscher Wetterdienst, cumulative sum over**  
**individual values. The storm analysis was performed by segmenting the rainfall datasets by the acquisition**  
**dates of the aerial imagery being: T1, T2, and T3, the years before the cliff fall plotted in dark colors; T4**  
**the mean rainfall after, during and one year after the cliff fall in light green; and T5 and T6 the time**  
**intervals with increased erosion in light green and yellow. a) mean rainfall intensity with a diversity of**  
**680 durations for the analysed time intervals. b) discrete daily precipitation between 2011 and 2021. Dots**  
**highlight days with rainfall intensity exceeding 10 mm/h.**

685 Sediment transport by channelized debris flows is a common process in the studied catchment before the cliff fall  
event, but spatially confined to the widened dispersed debris flow channel (Figure 7, 2010-2012, 2012-2014).  
Similar to reports from the the Dolomite region (Italian Alps), debris flow initiation occurred at the outlet of a  
small basin where concentrated overland flow feeds an ephemeral channel that incised slope deposits (Berti and  
Simoni, 2005). Monitoring at the Swiss Alps suggest increased debris flow activity after a sudden sediment input  
from a rock avalanche or large landslide (Bennett et al., 2014; Baer et al., 2017; Frank et al., 2019). A numerical  
modelling by (Bennett et al., 2014), calibrated for a debris flow-prone catchment enhanced the key role of  
sediment supply in debris flow formation even in erosive catchments. Even if the model results in transport-limited  
690 behavior for more than half of the time, the supply-limited condition in the debris flow channel results in highly  
nonlinear sediment discharge as a function of runoff. The material detached by the cliff fall entrained older  
deposits at the upper channelized erosive debris channel, which we traced back to 1945 by the visual inspection  
of historical aerial imagery, increasing the amount of transported sediment downslope. Despite this, inferred  
trajectories of sediment waves from the visual inspection of temporal series of orthophotos, most likely coalescent  
695 debris flows, and bulk erosion patterns, evidence short travel distances (<500 m), promoting the sediment transfer  
within the slope morphodynamic zones but rarely reaching the outlet. Multiple debris flow events were visually  
identified on the orthophotos based on differences in color and granulometry, but a complete separation remains  
challenging. Recent debris flows numerical models emphasize the importance of the topography on the motion of  
debris flow and the role of retention basins and memory effects for the acceleration-deceleration stage of the flow  
700 (Qiao et al., 2023) and the spatial distribution of eroded volumes (Haas et al., 2020). The sediment storages and  
sinks (marked as (1), (2), (3), and (4) in Figure 7) at our study catchment spatially correspond to slope changes  
which might decrease flow energy and thus debris flow travel distances. The enhanced accumulation in this region

is clearly visualize in the decadal topographic change in Figure 9-left. Currently, these areas with at least 10 m of recently cumulated sediment remain prone to mobilization possibly extending the system relaxation times (Heckmann and Schwanghart, 2013).

Numerical models aiming to assess the role of changes in precipitation, runoff and air temperature on sediment yield and debris flow activity based on climatic predictions suggest a reduction in both sediment supply and debris-flow, while identified sediment input into the sediment cascades as key parameter for debris flow activity (Hirschberg et al., 2021). The presented results exemplify how sediment input produced by a cliff fall resulted in the sediment continuity from the rockface to the outlet, however, the degree of continuity measured as the negative net change decrease considerable during the four years after the cliff fall (Figure 6 right). The results align with recent observations on the key role of sediment supply in landscape connectivity (Heckmann and Schwanghart, 2013), sediment continuity (Joyce et al., 2018) and debris flow occurrences (Bennett et al., 2013; Baer et al., 2017; Hirschberg et al., 2021; Battista et al., 2022). Remaining key questions deals with the interactions of sediment supply and hydrological conditions and the timing and mechanisms, e.g., sediment exhaustion, required to reestablish the pre-event morphodynamics where the rockface is decoupled from the fluvial system. Predictions on the sediment cascades at the Hochvogel required a deeper understanding on the rockfall triggering factors and rates of sediment production, currently object of research. On the other hand, sediment storages resulting from geomorphic processes such as high magnitude slope instability and paraglacial and glacier sediment storages, are often landforms decoupled from the present-day geomorphic process, therefore, studying the conditions that leads to increased sediment transport and reconnection of those systems support the prediction of geomorphic impact under a changing climate.

The fast system reaction time of 1 to 2 years is evidenced by the massive inversion from a depositional regimen (2015-2017) to an erosive regime (2017-2018) which mobilizes sediment through the system with short temporal residence times in the sediment cascading. The material detached by the cliff fall entrained older deposits at the upper channelized erosive debris channel, which we traced back to 1945 by the visual inspection of historical aerial imagery, increasing the amount of transported sediment downslope. Despite the remobilization of older deposits, more than 10 m of recently deposited sediment remains at the upper channelized debris channel which serves as a source for future debris flows and possibly extends the system relaxation times. Observations in the Swiss Alps suggest increased debris flow activity after a sudden sediment input from a rock avalanche or large landslides (Baer et al., 2017; Frank et al., 2019). Debris flows are a common process in the studied catchment before the cliff fall event, but spatially confined to the widened dispersed debris flow channel where sediment availability is high. On the contrary, increased sediment remobilization is clearly triggered at the upper channelized erosive debris flow channel shortly after the cliff fall, acting as an efficient process to restore sediment continuity, according to recent numerical simulations (Heckmann and Schwanghart, 2013) as the main mechanism of sediment transport in the studied catchment is debris flows.

Observations in the Swiss Alps suggest increased debris flow activity after a sudden sediment input from a rock avalanche or large landslides (Baer et al., 2017; Frank et al., 2019). Debris flows are a common process in the studied catchment before the cliff fall event, but spatially confined to the widened dispersed debris flow channel where sediment availability is high. On the contrary, increased sediment remobilization is clearly triggered at the

~~upper channelized erosive debris flow channel shortly after the cliff fall, acting as an efficient process to restore sediment continuity. A systematic study of six catchments in Switzerland affected by landslides that generated new sediment deposits suggests a considerable increase in debris flow frequency for one to eight years following the landslide with no clear rain fall related apparent trigger (Frank et al., 2019). For the studied catchment, relaxation times exceed the observation time thus we plan to continue with the monitoring.~~

745

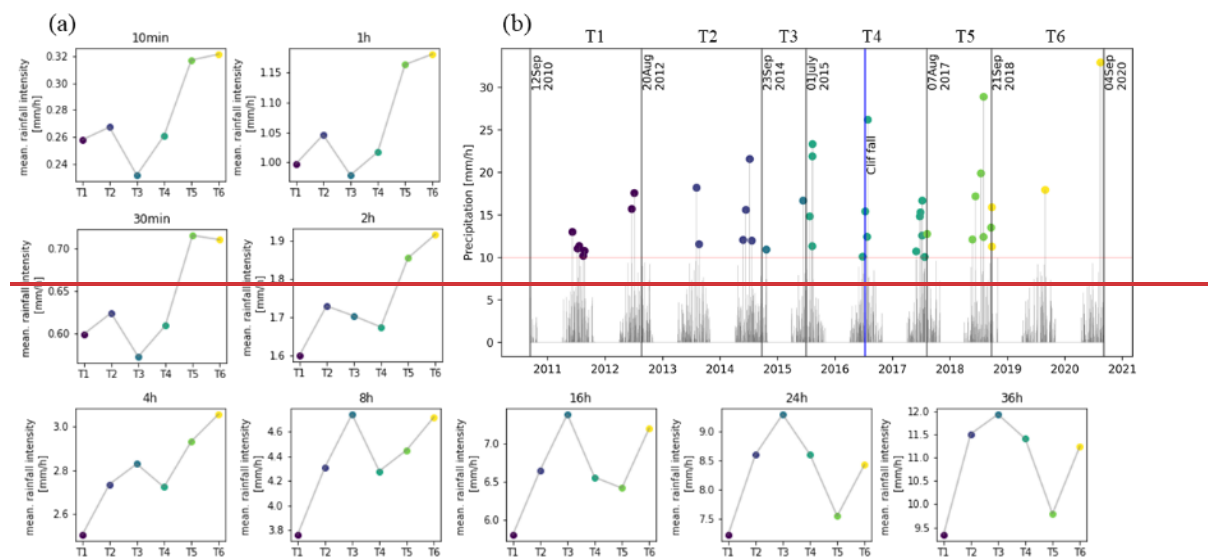
~~Debris flows are normally triggered by short duration and high intensity rainstorms. A study in the Zermatt Valley (Swiss Alps) concluded that the occurrence of debris flows would depend on short term changes in triggering rainfall rather than on long term climatic changes (Bollschweiler and Stoffel, 2010), thus high resolution temporal and spatial analysis are paramount to better assess the cascading natural hazard of rock slope failures. A review of nine debris flow monitored sites around the world suggests that hourly rainfall intensities between 5 and 15 mm/h are sufficient to trigger debris flows (Hürlimann et al., 2019). Particularly, at Illgraben basin, Switzerland, sediment transport was reported at rainfall intensity of 2.2 mm/10 min while debris flows were initiated in a range between 3.8 to 9.6 mm/10 min. Precipitation stations at the vicinity of the Hochvogel (Hinterhornbach/AUS—Station ID:6290) display increased mean seasonal (April November) rainfall intensity over the last decade for events with a duration less than 4 hours (Figure 9). The frequency of rainstorms exceeding 10mm/h, 3.8 mm/10min, and 9.6mm/10min are higher for the time interval when the cliff fall occurred (2015–2017: T4). The marked depositional regimen obscures the possible within slope impact of rainstorm increased frequency on debris flow activity, nonetheless, it might be reflected in the Joehbach stream power to erode the almost 3-meter terrace that incipiently blocked the outlet, preventing the blockade of the river system. Even though the massive erosive regimen subsequent to the cliff fall is characterized by rainfall frequencies similar to those pre-cliff falls (6 to 7 days with more than 10mm/h), the increased mean rainstorm intensity might play a role in the fast response times of the system.~~

750

755

760

765



~~Figure 9. Intensity-duration and frequency analysis for a diversity of rainfall events measured at the precipitation station 6290-Hinterhornbach/AUS. Data basis: Deutscher Wetterdienst, cumulative sum over individual values. The storm analysis was performed by segmenting the rainfall datasets by the acquisition dates of the aerial imagery being: T1, T2, and T3, the years before the cliff fall plotted in dark colors; T4~~

770



~~the mean rainfall after, during and one year after the cliff fall in light green; and T5 and T6 the time intervals with increased erosion in light green and yellow.~~

775 Debris flow inferred trajectories evidence short travel distances (<500 m) promoting the sediment transfer within the slope morphodynamic components but rarely reaching the outlet. Empirical relationships express the runout distance of debris flows in terms of topography and volume of mass (Rickenmann, 2005; Hürlimann et al., 2008). Sediment storages and sinks (marked as (1), (2), (3), and (4) in Figure 7) spatially correspond to slope changes that decrease flow energy thus debris flow travel distances. Regardless of the temporal lumping, multiple debris flow events were visually identified on the orthophotos based on differences in color and granulometry, but a complete separation remains challenging.

780 The formation of at least three levels of terraces with predominance coarse sediment after the cliff fall evidence the fluvial response to the decreased sediment flux at the outlet. The channelization of the river channel increases the stream erosion power thus possible lateral erosion downstream. Hence, the effects of the cliff fall event are seen not only in the higher erosive regimen at the hillslope but also in the morphodynamic adjustment of the Jochbach river. A remaining key question deals with the conditions, mechanism, and timing required to reestablish the pre-event morphodynamics. Currently, sediment storages resulting from geomorphic processes such as high magnitude slope instability and paraglacial and glacier sediment storages, are often landforms decoupled from the present-day geomorphic process. In the context of increased rainfall activity, the couple/reconnection of those systems and their magnitude and persistence will become key parameters for the management and development of alpine communities.

785  
790

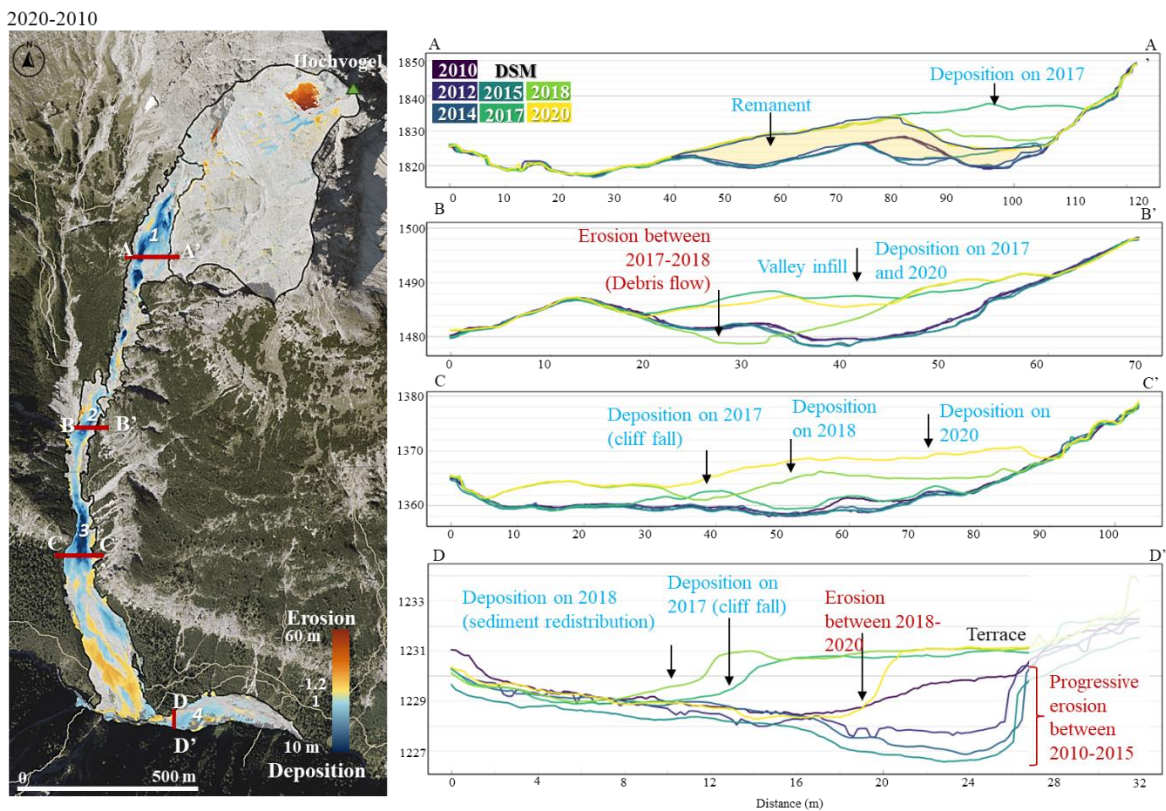


**Figure 9. Left. Decadal topographic change. Right. Topographic profiles at retention basins. Left: Cumulative topographic changes between 2010 and 2020. Dark blue areas indicate remaining sediment deposits with more than**

795 10m in elevation. Profile A-A' shows the formation of a depositional geform (sediment talus) which is partially  
eroded in the next few years. Blue polygon highlights the remanent sediment wedge with a depth of c.a. 10 m. Profile  
B-B' is located in the transfer zone between the Weittal valley and the lower valley. The confined valley is filled with  
800 sediment transferred from the cliff fall in 2017, partially eroded between 2017-2018, and filled again with sediment  
produced by secondary rockfalls and debris flows in 2020. Profile C-C' exhibits the dynamic of the confined fan apex  
which is slightly affected by the primary sediment produced during the cliff event but heavily impacted by the  
cascades. Progressive aggradation since 2017 evidenced the sediment waves in the system. Profile D-D', shows the  
formation and current erosion of a terrace formed as a result of the sediment that reached the outlet of the  
Wildenbach catchment. An initial sediment wave blocked partially the Jochbach river by c.a. 3 m of sediment.  
805 Additional sediment was annexed to the terrace in 2018. Currently, a remnant of 3 m. width is observed, less than  
half of the original terrace.

## 6. Conclusions

The combination of seismic information and temporal series of high-resolution wide-extent true-orthophotos and  
DSMs provide an accurate assessment of the temporal and special evolution of rockfalls and the subsequent  
810 massive sediment redistribution. A multi-stage detachment of more than 150,000 m<sup>3</sup> in the Hochvogel summit,  
northern calcareous alps (DE/AT), was responsible for the production of 97% of the total sediment eroded between  
2010 and 2020. We identified a significant disproportion in the contribution of rockfall magnitudes for the four  
slopes that constitute the summit with predominance of debris falls for the northern and western slopes, while the  
southeaster slope has a large proportion of boulder fall, thus, increased hazard. The seismic analysis revealed  
815 consecutive blockfalls with increased magnitude from 10<sup>3</sup> to 10<sup>4</sup> m<sup>3</sup> in a time period of 3 days during the summer  
of 2016, strongly increasing the rockfall risk in the area. Therefore, these results enhance the need of monitoring  
alpine slopes to better assess possible increased rockfall activity that leads to safety concerns. We suggest the  
integration of wide-extend photogrammetric datasets in future alpine early warning system.

820 The time series of spatial distribution of differences of DSM and differentiated geomorphic sediment budgets  
contributes to a better understanding of the complex nature and feedback of cascading processes. The alpine  
catchment quickly responded to the cliff fall within 0 to 4 years, resulting in massive sediment redistribution  
within the catchment and reduction in sediment delivery to the outlet. This, in turn, modified the fluvial response  
at the catchment outlet. Sediment continuity/transfer within the hillslope was rapidly recovered two years  
825 following the cliff fall. The recovered sediment flux mobilizes sediment along the geomorphic subsystems;  
however, the sediment waves were inefficient in delivering sediment to the catchment outlet. Relaxation times are  
expected beyond 10 years given that the latest observations (2020) still revealed perturbation in the system and  
the deposition of up to 10 m of sediment at the upper channelized debris flow which serves as a sediment input  
for future debris flows.

830

The results present the first step towards a better understanding, prediction, and early warning of alpine natural  
hazards under expected extreme climatic conditions. The ongoing interdisciplinary AlpSenseRely project aims to  
integrate high-resolution multi-scale, multi-temporal remote sensing data (Large format digital aerial  
photogrammetry and UAV) for an accurate quantification of temporal and spatial changes in alpine geomorphic  
835 systems.

## Data Availability

The original aerial imagery is available at Landesamt für Digitalisierung, Breitband und Vermessung (LDBV), Bundesamt für Eich- und Vermessungswesen (BEV), and 3D RealityMaps GmbH upon request. Precipitation data is freely available at the Geoportal from the Deutscher Wetterdienst (<https://dwd-geoportal.de/>). Seismic data is  
840 freely available at reported sources in the supplementary material.

## Author contributions

N.B. wrote the manuscript with contributions from J.L.

N.B. developed the topographic time series workflow, analyzed the data and compiled results

J.L. calculated seismic volumes

845 J.J. created DSM and orthophotos from digital aerial imagery

M.D. verified and advised on the implementation of the seismic volume's calculation

U.M, F.S and M.K provided guidance and funding

All authors checked and revised the text and the figures of the manuscript and contributed to the ideas developed in this study.

## 850 Competing interests

An author is a member of the editorial board of the journal Earth Surface Dynamics. The peer-review process was guided by an independent editor, and the authors have also no other competing interest to declare.

## Acknowledgments

We thank the Land Tyrol and particularly Mag. Thomas Figl for the open sharing of the pictures taken during the  
855 aerial inspection of the Hochvogel before the cliff fall which helped us to better picture the magnitude of the detachment, the Landslide research group at TUM for the fieldwork support during the UAV acquisitions, particularly to Andreas Dietrich for the UAV acquisition on 2017. [The publication of this work was financially supported by the Ludwig-Maximilians-University \(LMU\) through the 'Open Access Publishing' program.](#) We are indebted to Peter Mederer for his contribution to the early developments of the 3D-coregistration python workflow  
860 during his internship at 3D RealityMaps GmbH, and the colleagues at 3D RealityMaps GmbH, Munich for the outstanding support with the implementation of the 3D models used for visualization, visual interpretation, and figures. [We would like to thank the anonymous reviewer for the time devoted to the manuscript and special thanks to Dr. Georgina Bennett for the constructive comments to improve the quality of the manuscript.](#)

## 865 Financial support

This research was funded by the Bavarian [State Ministry of the Environment and Consumer Protection \(StMUV\)](#) in the framework of the project "AlpSenseRely" Alpine remote sensing of climate-induced natural hazards: Reliability of multi-method hazard prediction in a changing climate (Teilprojekt [for LMU TUSO1UFS-77318](#)). Initial datasets were acquired during the project 'AlpSenseBench' Alpine remote sensing of climate-induced  
870 natural hazards funded by the Bavarian [State Ministry for Economic Affairs, Regional Development and Energy \(StMWI\)](#) (grant no. 45-6723a/15/2).

## References

Abellán, A., Jaboyedoff, M., Oppikofer, T., and Vilaplana, J. M.: Detection of millimetric deformation using a terrestrial laser scanner: experiment and application to a rockfall event, Nat Hazard Earth Sys, 9, 365–372,  
875 <https://doi.org/10.5194/nhess-9-365-2009>, 2009.

- Anderson, S. W.: Uncertainty in quantitative analyses of topographic change: error propagation and the role of thresholding, *Earth Surf Processes*, 44, 1015–1033, <https://doi.org/10.1002/esp.4551>, 2019.
- Baer, P., Huggel, C., McArdell, B. W., and Frank, F.: Changing debris flow activity after sudden sediment input: a case study from the Swiss Alps, *Geology Today*, 33, 216–223, <https://doi.org/10.1111/gto.12211>, 2017.
- 880 Battista, G., Schlunegger, F., Burlando, P., and Molnar, P.: Sediment Supply Effects in Hydrology-Sediment Modeling of an Alpine Basin, *Water Resour Res*, 58, <https://doi.org/10.1029/2020wr029408>, 2022.
- Becht, M., Haas, F., Heckmann, T., and Wichmann, V.: A new modelling approach to delineate the spatial extent of alpine sediment cascades, *Geomorphology*, 111, 70–78, <https://doi.org/10.1016/j.geomorph.2008.04.028>, 2009.
- 885 Benda, L. E. and Dunne, T.: Stochastic Forcing of Sediment Routing and Storage in Channel Networks, *Water Resources Research*, 33, 2865–2880, <https://doi.org/10.1029/97wr02387>, 1997.
- Benjamin, J., Rosser, N. J., and Brain, M. J.: Emergent characteristics of rockfall inventories captured at a regional scale, *Earth Surf Processes*, 45, 2773–2787, <https://doi.org/10.1002/esp.4929>, 2020.
- 890 Bennett, G. L., Molnar, P., Eisenbeiss, H., and McArdell, B. W.: Erosional power in the Swiss Alps: characterization of slope failure in the Illgraben, *Earth Surf. Process. Landforms*, 37, 1627–1640, <https://doi.org/10.1002/esp.3263>, 2012.
- Bennett, G. L., Molnar, P., McArdell, B. W., Schlunegger, F., and Burlando, P.: Patterns and controls of sediment production, transfer and yield in the Illgraben, *Geomorphology*, 188, 68–82, <https://doi.org/10.1016/j.geomorph.2012.11.029>, 2013.
- 895 Bennett, G. L., Molnar, P., McArdell, B. W., and Burlando, P.: A probabilistic sediment cascade model of sediment transfer in the Illgraben, *Water Resour Res*, 50, 1225–1244, <https://doi.org/10.1002/2013wr013806>, 2014.
- Berger, C., McArdell, B. W., and Schlunegger, F.: Sediment transfer patterns at the Illgraben catchment, Switzerland: Implications for the time scales of debris flow activities, *Geomorphology*, 125, 421–432, <https://doi.org/10.1016/j.geomorph.2010.10.019>, 2011.
- 900 Berti, M. and Simoni, A.: Experimental evidences and numerical modelling of debris flow initiated by channel runoff, *Landslides*, 2, 171–182, <https://doi.org/10.1007/s10346-005-0062-4>, 2005.
- Bollschweiler, M. and Stoffel, M.: Changes and trends in debris-flow frequency since AD 1850: Results from the Swiss Alps, *Holocene*, 20, 907–916, <https://doi.org/10.1177/0959683610365942>, 2010.
- 905 Borselli, L., Cassi, P., and Torri, D.: Prolegomena to sediment and flow connectivity in the landscape: A GIS and field numerical assessment, *CATENA*, 75, 268–277, <https://doi.org/10.1016/j.catena.2008.07.006>, 2008.
- Bracken, L. J., Turnbull, L., Wainwright, J., and Bogaart, P.: Sediment connectivity: a framework for understanding sediment transfer at multiple scales, *Earth Surf Processes*, 40, 177–188, <https://doi.org/10.1002/esp.3635>, 2015.
- 910 Brown, A. G., Carey, C., Erkens, G., Fuchs, M., Hoffmann, T., Macaire, J.-J., Moldenhauer, K.-M., and Walling, D. E.: From sedimentary records to sediment budgets: Multiple approaches to catchment sediment flux, *Geomorphology*, 108, 35–47, <https://doi.org/10.1016/j.geomorph.2008.01.021>, 2009.
- Burt, T. P. and Allison, R. J.: *Sediment Cascades. An Integrated Approach*, First edition., John Wiley & Sons, Ltd, 2010.

- 915 Clapuyt, F., Vanacker, V., Christl, M., Oost, K. V., and Schlunegger, F.: Spatio-temporal dynamics of sediment transfer systems in landslide-prone Alpine catchments, *Solid Earth*, 10, 1489–1503, <https://doi.org/10.5194/se-10-1489-2019>, 2019.
- CloudCompare v2.0: A software for processing and comparing 3D point clouds: <http://www.cloudcompare.com>.
- 920 DAV, D.: Neue Felsstürze vom Hochvogel ins Weittal, Juli 2016 | Neue Felsstürze vom Hochvogel ins Weittal, 2016.
- DAV, D.: Chronik - Sperrung des Bäumenheimer Weges, Sperrung Bäumenheimer Weg, 2017.
- Dietrich, W. E., Dunne, T., Humphrey, N. F., and Reid, L. M.: Construction of sediment budgets for drainage basins, in: Construction of sediment budgets for drainage basins, vol. 141, 5–23, 1982.**
- 925 Dietze, M., Mohadjer, S., Turowski, J. M., Ehlers, T. A., and Hovius, N.: Seismic monitoring of small alpine rockfalls – validity, precision and limitations, *Earth Surf Dynam*, 5, 653–668, <https://doi.org/10.5194/esurf-5-653-2017>, 2017a.
- Dietze, M., Turowski, J. M., Cook, K. L., and Hovius, N.: Spatiotemporal patterns, triggers and anatomies of seismically detected rockfalls, *Earth Surf Dynam*, 5, 757–779, <https://doi.org/10.5194/esurf-5-757-2017>, 2017b.
- 930 Dietze, M., Krautblatter, M., Illien, L., and Hovius, N.: Seismic constraints on rock damaging related to a failing mountain peak: the Hochvogel, Allgäu, *Earth Surf. Process. Landforms*, 46, 417–429, <https://doi.org/10.1002/esp.5034>, 2021.
- Draebing, D., Mayer, T., Jacobs, B., and McColl, S. T.: Alpine rockwall erosion patterns follow elevation-dependent climate trajectories, *Commun Earth Environ*, 3, 21, <https://doi.org/10.1038/s43247-022-00348-2>, 2022.
- 935 Dussauge-Peisser, C., Helmstetter, A., Grasso, J.-R., Hantz, D., Desvarreux, P., Jeannin, M., and Giraud, A.: Probabilistic approach to rock fall hazard assessment: potential of historical data analysis, *Nat Hazard Earth Sys*, 2, 15–26, <https://doi.org/10.5194/nhess-2-15-2002>, 2002.
- 940 Eltner, A. and Sofia, G.: Structure from motion photogrammetric technique, in: *Developments in Earth surface process*, vol. 23, edited by: Tarolli, P. and Mudd, S. M., 1–24, <https://doi.org/10.1016/b978-0-444-64177-9.00001-1>, 2020.
- Erismann, T. H. and Abele, G.: *Dynamics of Rockslides and Rockfalls*, Springer Science & Business Media, Heidelberg, 2001.
- Fabris, M. and Pesci, A.: Automated DEM extraction in digital aerial photogrammetry: precisions and validation for mass movement monitoring, *Ann Geophys-italy*, 48, <https://doi.org/10.4401/ag-3247>, 2009.
- 945 **Fawcett, D., Blanco-Sacristán, J., and Benaud, P.: Two decades of digital photogrammetry: Revisiting Chandler’s 1999 paper on “Effective application of automated digital photogrammetry for geomorphological research” – a synthesis, *Prog Phys Geogr Earth Environ*, 43, 299–312, <https://doi.org/10.1177/0309133319832863>, 2019.**
- 950 Fischer, L., Purves, R. S., Huggel, C., Noetzli, J., and Haerberli, W.: On the influence of topographic, geological and cryospheric factors on rock avalanches and rockfalls in high-mountain areas, *Nat Hazard Earth Sys*, 12, 241–254, <https://doi.org/10.5194/nhess-12-241-2012>, 2012.
- Frank, F., Huggel, C., McArdell, B. W., and Vieli, A.: Landslides and increased debris-flow activity: A systematic comparison of six catchments in Switzerland, *Earth Surf Processes*, 44, 699–712, <https://doi.org/10.1002/esp.4524>, 2019.



- 955 Fryirs, K.: (Dis)Connectivity in catchment sediment cascades: a fresh look at the sediment delivery problem, *Earth Surf Processes*, 38, 30–46, <https://doi.org/10.1002/esp.3242>, 2013.
- Fuchs, F., Lenhardt, W., Bokelmann, G., and Group, the A. W.: Seismic detection of rockslides at regional scale: examples from the Eastern Alps and feasibility of kurtosis-based event location, *Earth Surf Dynam*, 6, 955–970, <https://doi.org/10.5194/esurf-6-955-2018>, 2018.
- 960 Geissler, J., Mayer, C., Jubanski, J., Münzer, U., and Siegert, F.: Analyzing glacier retreat and mass balances using aerial and UAV photogrammetry in the Ötztal Alps, Austria, *Cryosphere*, 15, 3699–3717, <https://doi.org/10.5194/tc-15-3699-2021>, 2021.
- Gregory, K. J. and Lewin, J.: *The Basics of Geomorphology: Key Concepts*, <https://doi.org/10.4135/9781473909984>, 2014.
- 965 Guerin, A., Ravanel, L., Matasci, B., Jaboyedoff, M., and Deline, P.: The three-stage rock failure dynamics of the Drus (Mont Blanc massif, France) since the June 2005 large event, *Sci Rep-uk*, 10, 17330, <https://doi.org/10.1038/s41598-020-74162-1>, 2020.
- Haala, N. and Rothemel, M.: Dense Multi-Stereo Matching for High Quality Digital Elevation Models, *Photogrammetrie - Fernerkundung - Geoinformation*, 2012, 331–343, <https://doi.org/10.1127/1432-8364/2012/0121>, 2012.
- 970 Haas, T. de, Nijland, W., Jong, S. M. de, and McArdell, B. W.: How memory effects, check dams, and channel geometry control erosion and deposition by debris flows, *Sci. Rep.*, 10, 14024, <https://doi.org/10.1038/s41598-020-71016-8>, 2020.
- Hantz, D., Corominas, J., Crosta, G. B., and Jaboyedoff, M.: Definitions and Concepts for Quantitative Rockfall Hazard and Risk Analysis, *Geosciences*, 11, 158, <https://doi.org/10.3390/geosciences11040158>, 2021.
- 975 Harvey, A. M.: Coupling between hillslopes and channels in upland fluvial systems: implications for landscape sensitivity, illustrated from the Howgill Fells, northwest England, *CATENA*, 42, 225–250, [https://doi.org/10.1016/s0341-8162\(00\)00139-9](https://doi.org/10.1016/s0341-8162(00)00139-9), 2001.
- Heckmann, T. and Schwanghart, W.: Geomorphic coupling and sediment connectivity in an alpine catchment — Exploring sediment cascades using graph theory, *Geomorphology*, 182, 89–103, <https://doi.org/10.1016/j.geomorph.2012.10.033>, 2013.
- 980 Heckmann, T., Bimböse, M., Krautblatter, M., Haas, F., Becht, M., and Morche, D.: From geotechnical analysis to quantification and modelling using LiDAR data: a study on rockfall in the Reintal catchment, Bavarian Alps, Germany, *Earth Surf Processes*, 37, 119–133, <https://doi.org/10.1002/esp.2250>, 2012.
- 985 Heckmann, T., Hilger, L., Vehling, L., and Becht, M.: Integrating field measurements, a geomorphological map and stochastic modelling to estimate the spatially distributed rockfall sediment budget of the Upper Kaunertal, Austrian Central Alps, *Geomorphology*, 260, 16–31, <https://doi.org/10.1016/j.geomorph.2015.07.003>, 2016.
- Heißel, G. and Figl, T.: *Stellungnahme der Amtssachverständigen für Geologie, Hydrogeologie und technische Geologie, sowie für den Schutz vor Erosion und vor alpinen geogenen Naturgefahren*, 2017.
- 990 Hibert, C., Mangeney, A., Grandjean, G., and Shapiro, N. M.: Slope instabilities in Dolomieu crater, Réunion Island: From seismic signals to rockfall characteristics, *J Geophys Res Earth Surf*, 116, <https://doi.org/10.1029/2011jf002038>, 2011.
- Hilger, L. and Beylich, A. A.: Geomorphology of Proglacial Systems, Landform and Sediment Dynamics in Recently Deglaciated Alpine Landscapes, *Geogr Phys Environ*, 251–269, [https://doi.org/10.1007/978-3-319-94184-4\\_15](https://doi.org/10.1007/978-3-319-94184-4_15), 2018.
- 995

- Hirschberg, J., Faticchi, S., Bennett, G. L., McArdeell, B. W., Peleg, N., Lane, S. N., Schlunegger, F., and Molnar, P.: Climate Change Impacts on Sediment Yield and Debris-Flow Activity in an Alpine Catchment, *J. Geophys. Res.: Earth Surf.*, 126, <https://doi.org/10.1029/2020jf005739>, 2021.
- 1000 Hirschmüller, H.: Stereo Processing by Semiglobal Matching and Mutual Information, *Ieee T Pattern Anal*, 30, 328–341, <https://doi.org/10.1109/tpami.2007.1166>, 2008.
- Hungr, O., McDougall, S., Wise, M., and Cullen, M.: Magnitude–frequency relationships of debris flows and debris avalanches in relation to slope relief, *Geomorphology*, 96, 355–365, <https://doi.org/10.1016/j.geomorph.2007.03.020>, 2008.
- 1005 Hürlimann, M., Rickenmann, D., Medina, V., and Bateman, A.: Evaluation of approaches to calculate debris-flow parameters for hazard assessment, *Eng Geol*, 102, 152–163, <https://doi.org/10.1016/j.enggeo.2008.03.012>, 2008.
- Hürlimann, M., Coviello, V., Bel, C., Guo, X., Berti, M., Graf, C., Hübl, J., Miyata, S., Smith, J. B., and Yin, H.-Y.: Debris-flow monitoring and warning: review and examples, *Earth-sci Rev*, 199, 102981, <https://doi.org/10.1016/j.earscirev.2019.102981>, 2019.
- 1010 Jakob, M.: A size classification for debris flows, *Eng Geol*, 79, 151–161, <https://doi.org/10.1016/j.enggeo.2005.01.006>, 2005.
- James, L. A., Hodgson, M. E., Ghoshal, S., and Latiolais, M. M.: Geomorphic change detection using historic maps and DEM differencing: The temporal dimension of geospatial analysis, *Geomorphology*, 137, 181–198, <https://doi.org/10.1016/j.geomorph.2010.10.039>, 2012.
- 1015 Joyce, H. M., Hardy, R. J., Warburton, J., and Large, A. R. G.: Sediment continuity through the upland sediment cascade: geomorphic response of an upland river to an extreme flood event, *Geomorphology*, 317, 45–61, <https://doi.org/10.1016/j.geomorph.2018.05.002>, 2018.
- Kaufmann, V. and Ladstädter, R.: Quantitative analysis of rock glacier creep by means of digital photogrammetry using multi-temporal aerial photographs: Two case studies in the Austrian Alps, in: Proceedings of the 8th International Conference on Permafrost, 525–530, 2003.
- 1020 Kazhdan, M., Chuang, M., Rusinkiewicz, S., and Hoppe, H.: Poisson Surface Reconstruction with Envelope Constraints, *Comput Graph Forum*, 39, 173–182, <https://doi.org/10.1111/cgf.14077>, 2020.
- Korup, O., Densmore, A. L., and Schlunegger, F.: The role of landslides in mountain range evolution, *Geomorphology*, 120, 77–90, <https://doi.org/10.1016/j.geomorph.2009.09.017>, 2010.
- 1025 Krautblatter, M., Moser, M., Schrott, L., Wolf, J., and Morche, D.: Significance of rockfall magnitude and carbonate dissolution for rock slope erosion and geomorphic work on Alpine limestone cliffs (Reintal, German Alps), *Geomorphology*, 167, 21–34, <https://doi.org/10.1016/j.geomorph.2012.04.007>, 2012.
- Kromer, R., Lato, M., Hutchinson, D. J., Gauthier, D., and Edwards, T.: Managing rockfall risk through baseline monitoring of precursors using a terrestrial laser scanner, *Can Geotech J*, 54, 953–967, <https://doi.org/10.1139/cgj-2016-0178>, 2017.
- 1030 Kromer, R. A., Rowe, E., Hutchinson, J., Lato, M., and Abellán, A.: Rockfall risk management using a pre-failure deformation database, *Landslides*, 15, 847–858, <https://doi.org/10.1007/s10346-017-0921-9>, 2018.
- Lacroix, P. and Helmstetter, A.: Location of Seismic Signals Associated with Microearthquakes and Rockfalls on the Séchilienne Landslide, French Alps, *Location of Seismic Signals Associated with Microearthquakes and Rockfalls on Séchilienne Landslide*, *B Seismol Soc Am*, 101, 341–353, <https://doi.org/10.1785/0120100110>, 2011.
- 1035

- Leinauer, J., Jacobs, B., and Krautblatter, M.: Anticipating an imminent large rock slope failure at the Hochvogel (Allgäu Alps), *Geomechanics Tunn*, 13, 597–603, <https://doi.org/10.1002/geot.202000027>, 2020.
- 1040 Leinauer, J., Jacobs, B., and Krautblatter, M.: High alpine geotechnical real time monitoring and early warning at a large imminent rock slope failure (Hochvogel, GER/AUT), *Iop Conf Ser Earth Environ Sci*, 833, 012146, <https://doi.org/10.1088/1755-1315/833/1/012146>, 2021.
- Le Roy, G., Helmstetter, A., Amitrano, D., Guyoton, F., and Roux-Mallouf, R. L.: Seismic Analysis of the Detachment and Impact Phases of a Rockfall and Application for Estimating Rockfall Volume and Free-Fall Height, *J Geophys Res Earth Surf*, 124, 2602–2622, <https://doi.org/10.1029/2019jf004999>, 2019.
- 1045
- Manconi, A., Picozzi, M., Coviello, V., Santis, F. D., and Elia, L.: Real-time detection, location, and characterization of rockslides using broadband regional seismic networks, *Geophys Res Lett*, 43, 6960–6967, <https://doi.org/10.1002/2016gl069572>, 2016.
- 1050 Marzolf, I. and Poesen, J.: The potential of 3D gully monitoring with GIS using high-resolution aerial photography and a digital photogrammetry system, *Geomorphology*, 111, 48–60, <https://doi.org/10.1016/j.geomorph.2008.05.047>, 2009.
- McSaveney, M. J.: Recent rockfalls and rock avalanches in Mount Cook National Park, New Zealand, in: *Catastrophic Landslides Effects, occurrences and Mechanisms*, vol. XV, Geological Society of America, <https://doi.org/10.1130/reg15>, 2002.
- 1055 Mergili, M., Jaboyedoff, M., Pullarello, J., and Pudasaini, S. P.: Back calculation of the 2017 Piz Cengalo–Bondo landslide cascade with r.avaflow: what we can do and what we can learn, *Nat Hazard Earth Sys*, 20, 505–520, <https://doi.org/10.5194/nhess-20-505-2020>, 2020.
- Micheletti, N., Lane, S. N., and Chandler, J. H.: Application of archival aerial photogrammetry to quantify climate forcing of alpine landscapes, *Photogrammetric Rec*, 30, 143–165, <https://doi.org/10.1111/phor.12099>, 2015.
- 1060
- NNZ: Die Murgänge bei Bondo kosten rund 41 Millionen Franken, , 14th December, 2017.
- Owens, P. N., Peticrew, E. L., and Perk, M. van der: Sediment response to catchment disturbances, *J Soils Sediments*, 10, 591–596, <https://doi.org/10.1007/s11368-010-0235-1>, 2010.
- 1065 Qiao, Z., Li, T., Simoni, A., Gregoret, C., Bernard, M., Wu, S., Shen, W., and Berti, M.: Numerical modelling of an alpine debris flow by considering bed entrainment, *Front. Earth Sci.*, 10, 1059525, <https://doi.org/10.3389/feart.2022.1059525>, 2023.
- Rickenmann, D.: *Debris-flow Hazards and Related Phenomena*, Springer Praxis Books, 305–324, [https://doi.org/10.1007/3-540-27129-5\\_13](https://doi.org/10.1007/3-540-27129-5_13), 2005.
- Riggs, H. C.: *Frequency Curves*, US Government Printing Office, 1968.
- 1070 Rosser, N., Lim, M., Petley, D., Dunning, S., and Allison, R.: Patterns of precursory rockfall prior to slope failure, *J Geophys Res Earth Surf* 2003 2012, 112, <https://doi.org/10.1029/2006jf000642>, 2007.
- Rothermel, Mathias., Wenzel, K., Fritsch, D., and Haala, N.: SURE: Photogrammetric surface reconstruction from imagery, in: *Proceedings LC3D Workshop*, 615–620, 2012.
- 1075 ~~Le Roy, G., Helmstetter, A., Amitrano, D., Guyoton, F., and Roux-Mallouf, R. L.: Seismic Analysis of the Detachment and Impact Phases of a Rockfall and Application for Estimating Rockfall Volume and Free-Fall Height, *J Geophys Res Earth Surf*, 124, 2602–2622, <https://doi.org/10.1029/2019jf004999>, 2019.~~

- Savi, S., Buter, A., Heckmann, T., Theule, J., Mao, L., and Comiti, F.: Multi-temporal analysis of morphological changes in an Alpine proglacial area and their effect on sediment transfer, *Catena*, 220, 106701, <https://doi.org/10.1016/j.catena.2022.106701>, 2023.
- 1080 Schiefer, E. and Gilbert, R.: Reconstructing morphometric change in a proglacial landscape using historical aerial photography and automated DEM generation, *Geomorphology*, 88, 167–178, <https://doi.org/10.1016/j.geomorph.2006.11.003>, 2007.
- Schrott, L., Hufschmidt, G., Hankammer, M., Hoffmann, T., and Dikau, R.: Spatial distribution of sediment storage types and quantification of valley fill deposits in an alpine basin, Reintal, Bavarian Alps, Germany, *Geomorphology*, 55, 45–63, [https://doi.org/10.1016/s0169-555x\(03\)00131-4](https://doi.org/10.1016/s0169-555x(03)00131-4), 2003.
- 1085 Schwab, M., Rieke-Zapp, D., Schneider, H., Liniger, M., and Schlunegger, F.: Landsliding and sediment flux in the Central Swiss Alps: A photogrammetric study of the Schimbrig landslide, Entlebuch, *Geomorphology*, 97, 392–406, <https://doi.org/10.1016/j.geomorph.2007.08.019>, 2008.
- Theler, D., Reynard, E., Lambiel, C., and Bardou, E.: The contribution of geomorphological mapping to sediment transfer evaluation in small alpine catchments, *Geomorphology*, 124, 113–123, <https://doi.org/10.1016/j.geomorph.2010.03.006>, 2010.
- 1090 Thiele, S. T., Grose, L., Samsu, A., Micklethwaite, S., Vollgger, S. A., and Cruden, A. R.: Rapid, semi-automatic fracture and contact mapping for point clouds, images and geophysical data, *Solid Earth*, 8, 1241–1253, <https://doi.org/10.5194/se-8-1241-2017>, 2017.
- Tucker, G. E.: Drainage basin sensitivity to tectonic and climatic forcing: implications of a stochastic model for the role of entrainment and erosion thresholds, *Earth Surf Processes*, 29, 185–205, <https://doi.org/10.1002/esp.1020>, 2004.
- 1095 Walling, D. E.: The sediment delivery problem, *J Hydrol*, 65, 209–237, [https://doi.org/10.1016/0022-1694\(83\)90217-2](https://doi.org/10.1016/0022-1694(83)90217-2), 1983.
- 1100 Walling, D. E. and Collins, A. L.: The catchment sediment budget as a management tool, *Environ Sci Policy*, 11, 136–143, <https://doi.org/10.1016/j.envsci.2007.10.004>, 2008.
- Whalley, B.: The mechanics of high-magnitude low-frequency rock failure and its importance in a mountainous area, *Reading Geographical Papers*, 1974.
- Whalley, B.: Rockfalls, *Slope Instability*, Chapter 7, 1984.
- 1105 Wheaton, J. M., Brasington, J., Darby, S. E., and Sear, D. A.: Accounting for uncertainty in DEMs from repeat topographic surveys: improved sediment budgets, *Earth Surf Processes*, 35, 136–156, <https://doi.org/10.1002/esp.1886>, 2010.
- Wichmann, V., Heckmann, T., Haas, F., and Becht, M.: A new modelling approach to delineate the spatial extent of alpine sediment cascades, *Geomorphology*, 111, 70–78, <https://doi.org/10.1016/j.geomorph.2008.04.028>, 2009.
- 1110 Williams, J. G., Rosser, N. J., Hardy, R. J., and Brain, M. J.: The Importance of Monitoring Interval for Rockfall Magnitude-Frequency Estimation, *J Geophys Res Earth Surf*, 124, 2841–2853, <https://doi.org/10.1029/2019jf005225>, 2019.